The Astrophysical Journal, 988:246 (21pp), 2025 August 1 https://doi.org/10.3847/1538-4357/ade886

Environmental Evidence for Overly Massive Black Holes in Low-mass Galaxies and a Black Hole–Halo Mass Relation at $z \sim 5$

Jorryt Matthee[1], Rohan P. Naidu[2,20], Gauri Kotiwale[1], Lukas J. Furtak[3], Ivan Kramarenko[1], Ruari Mackenzie[4], Jenny Greene[5], Angela Adamo[6], Rychard J. Bouwens[7], Claudia Di Cesare[1], Anna-Christina Eilers[8,9], Anna de Graaff[10], Kasper E. Heintz[11,12,13], Daichi Kashino[14], Michael V. Maseda[15], Sandro Tacchella[16,17], and Alberto Torralba[1,18,19]

[1] Institute of Science and Technology Austria (ISTA), Am Campus 1, 3400 Klosterneuburg, Austria; jorryt.matthee@ista.ac.at
[2] MIT Kavli Institute for Astrophysics and Space Research, 70 Vassar Street, Cambridge, MA 02139, USA
[3] Department of Physics, Ben-Gurion University of the Negev, P.O. Box 653, Be'er-Sheva 84105, Israel
[4] Department of Physics, ETH Zürich, Wolfgang-Pauli-Strasse 27, Zürich, 8093, Switzerland
[5] Department of Astrophysical Sciences, Princeton University, Princeton, NJ 08544, USA
[6] The Oskar Klein Centre, Department of Astronomy, Stockholm University, AlbaNova, SE-10691 Stockholm, Sweden
[7] Leiden Observatory, Leiden University, NL-2300 RA Leiden, The Netherlands
[8] MIT Kavli Institute for Astrophysics and Space Research, 77 Massachusetts Avenue, Cambridge, MA 02139, USA
[9] Department of Physics, Massachusetts Institute of Technology, Cambridge, MA 02139, USA
[10] Max-Planck-Institut für Astronomie, Königstuhl 17, D-69117, Heidelberg, Germany
[11] Department of Astronomy, University of Geneva, Chemin Pegasi 51, 1290 Versoix, Switzerland
[12] Cosmic Dawn Center (DAWN), Copenhagen, Denmark
[13] Niels Bohr Institute, University of Copenhagen, Jagtvej 128, København N, DK-2200, Denmark
[14] National Astronomical Observatory of Japan, 2-21-1 Osawa, Mitaka, Tokyo 181-8588, Japan
[15] Department of Astronomy, University of Wisconsin-Madison, 475 N. Charter Street, Madison, WI 53706, USA
[16] Kavli Institute for Cosmology, University of Cambridge, Madingley Road, Cambridge CB3 0HA, UK
[17] Cavendish Laboratory, University of Cambridge, 19 JJ Thomson Avenue, Cambridge CB3 0HE, UK
[18] Observatori Astronòmic de la Universitat de València, Ed. Instituts d'Investigació, Parc Científic. C/ Catedrático José Beltrán, n2, 46980 Paterna, Valencia, Spain
[19] Departament d'Astronomia i Astrofísica, Universitat de València, 46100 Burjassot, Spain

Received 2024 December 4; revised 2025 June 24; accepted 2025 June 24; published 2025 July 29

Abstract

JWST observations have unveiled faint active galactic nuclei (AGNs) at high redshift that provide insights into the formation of supermassive black holes (SMBHs). However, disentangling their stellar from AGN light is challenging. Here, we use an empirical approach to infer the average stellar mass of five faint broad-line (BL) Hα emitters at $z = 4$–5 with BH masses $\approx 6 \times 10^6\,M_\odot$, with a method independent of their spectral energy distribution (SED). We use the deep JWST/NIRcam grism survey "All the Little Things" to measure the overdensities around BL-Hα emitters and around a spectroscopic reference sample of $\sim$300 galaxies. In our reference sample, we find that megaparsec-scale overdensity correlates with stellar mass. Their large-scale environments suggest that BL-Hα emitters are hosted by galaxies with stellar masses $\approx 5 \times 10^7\,M_\odot$, $\approx$40 times lower than those inferred from galaxy-only SED fits. Adding measurements around more luminous $z \approx 6$ AGNs, we find tentative correlations between line width, BH mass, and the overdensity, suggestive of a steep BH to halo mass relation. The main implications are (1) when BH masses are taken at face value, we confirm extremely high BH to stellar mass ratios of $\approx$10%, (2) the galaxies of low stellar mass that host growing SMBHs are in tension with typical hydrodynamical simulations, except those without feedback, (3) a 1% duty cycle implied by the host mass hints at super-Eddington accretion, (4) the masses are at odds with an interpretation of the line broadening in terms of high stellar density, (5) our results imply a luminosity-dependent diversity of galaxy masses, environments, and SEDs among AGN samples.

Unified Astronomy Thesaurus concepts: AGN host galaxies (2017); High-redshift galaxies (734); Early universe (435); Quasars (1319); Emission line galaxies (459); Galaxies (573)

1. Introduction

The rapid formation of supermassive black holes (SMBHs) in the early Universe and the role that feedback from active galactic nuclei (AGNs) has on galaxy formation are among the key questions in present-day extragalactic astrophysics. How could black holes with masses $\sim 10^{10}\,M_\odot$ (X.-B. Wu et al. 2015; A.-C. Eilers et al. 2023) emerge already by $z \approx 6$? How can we explain the seemingly high black hole to stellar mass ratio inferred in many distant AGNs (e.g., F. Pacucci et al. 2023)? Do these ratios indicate SMBH formation scenarios from nonstellar origin such as direct collapse (Z. Haiman 2013; P. Natarajan et al. 2024) or highly super-Eddington accretion (J. S. Bennett et al. 2024; F. Huško et al. 2025)? Is AGN feedback responsible for quenching the highest-redshift passive galaxies (A. C. Carnall et al. 2023; F. D'Eugenio et al. 2024; A. de Graaff et al. 2025c; A. Weibel et al. 2025)?

While the brightest AGNs above $z \gtrsim 4$, i.e., quasars, have been known for decades (see X. Fan et al. 2023 for a recent review), JWST has significantly expanded the parameter space

---

[20] NASA Hubble Fellow.

of known AGNs at high redshifts toward lower luminosities and black hole masses (A. Adamo et al. 2024; J. Scholtz et al. 2025; H. Treiber et al. 2025). JWST has also identified indications of AGN activity beyond redshifts $z > 8$ (V. Kokorev et al. 2023; A. D. Goulding et al. 2023; R. L. Larson et al. 2023; R. Maiolino et al. 2024b; L. Napolitano et al. 2025). Therefore, these new samples hold the promise of improving our understanding of the earliest stages of SMBH formation and growth.

The population of broad-line-selected AGNs at $z \sim 3$–8 (J. Matthee et al. 2024; X. Lin et al. 2024; J. E. Greene et al. 2024) has been a key focus of attention. A significant subset of these are compact, with red rest-frame optical colors, in particular those where the broad-line (BL) component is more dominant, leading J. Matthee et al. (2024) to nickname them Little Red Dots (LRDs). The term LRDs has more widely been used to describe galaxies with a range of selection criteria, such as V-shaped spectral energy distributions (SEDs) with blue UV and red optical continua (e.g., M. Killi et al. 2024; P. G. Pérez-González et al. 2024; I. Labbe et al. 2025) or compact red sources (H. B. Akins et al. 2024). The BL-selected samples contain both sources with blue UV colors and objects that are red in the rest UV to optical regime (J. Matthee et al. 2024). In this paper, we primarily focus on BL-Hα emitters.

What are BL-Hα emitters and what do they teach us about early SMBH formation? So far, most effort has been spent understanding the SEDs of LRDs and BL-Hα emitters in particular (e.g., P. G. Pérez-González et al. 2024; D. J. Setton et al. 2024a; Y. Ma et al. 2025; M. Volonteri et al. 2025). These SEDs include unusual features such as a flat rest-frame near-infrared SED that is suggesting the lack of the typical hot dust emission around AGNs (H. B. Akins et al. 2024; C. C. Williams et al. 2024; B. Wang et al. 2025), an extreme X-ray faintness (T. T. Ananna et al. 2024; D. D. Kocevski et al. 2025; M. Yue et al. 2024a; R. Maiolino et al. 2025), and the presence of Balmer absorption, suggesting very dense gas (I. Juodžbalis et al. 2024a; J. Matthee et al. 2024) that is possibly Compton-thick (K. Inayoshi & R. Maiolino 2025; R. Maiolino et al. 2025).

Among the key goals of the study of BL-Hα emitters has been to measure the stellar mass of their host galaxies, as the relationship between BH mass and host galaxy mass is one of the fundamental relations that encode the physics of SMBH formation and growth (e.g., Y. Harikane et al. 2023; L. J. Furtak et al. 2024; I. Juodžbalis et al. 2024b; V. Kokorev et al. 2024; R. Maiolino et al. 2024a; M. A. Marshall et al. 2024; M. Onoue et al. 2024; M. Yue et al. 2024a). These studies typically find very high SMBH mass to stellar mass ratios relative to the local $z = 0$ scaling relation (e.g., F. Pacucci et al. 2023), partly due to the selection effect whereby AGN activity is easier to measure in galaxies with more massive BHs (J. Li et al. 2025). However, accurately measuring their stellar masses is challenging (e.g., G. C. K. Leung et al. 2024). Without accounting for AGN light, stellar masses can easily be overestimated—indeed, some seemingly overmassive galaxies (I. Labbé et al. 2023) turn out to have a significant AGN component (see, e.g., D. D. Kocevski et al. 2023a; B. Wang et al. 2024). Reliably accounting for the AGN component is not straightforward, as the AGN SEDs are poorly understood (e.g., Y. Ma et al. 2025). In particular, dense gas whose presence is indicated by Balmer absorption may also produce a Balmer break (K. Inayoshi & R. Maiolino 2025), a spectral feature typically associated with ∼100 Myr old stellar populations, but seemingly ubiquitous among LRDs (D. J. Setton et al. 2024a). These challenges call for complementary approaches to characterize the galaxies with broad Hα.

In our paradigm of cosmic structure formation, it is well understood that the large-scale environments of galaxies are correlated with the properties of the dark matter halos hosting these galaxies, i.e., on average, more massive galaxies reside in larger overdensities because they are hosted by more massive dark matter halos (e.g., G. R. Blumenthal et al. 1984). Abundance-matching studies of high-redshift galaxies have confirmed the existence of a strong stellar mass–halo mass relation out to $z \sim 10$ (e.g., M. Shuntov et al. 2025a), and clustering measurements based on photometric redshifts show indications of a luminosity-dependent bias (N. Dalmasso et al. 2024). The environments of luminous quasars at $z \sim 6$ suggest that they, on average, reside in halos with masses $\approx 3 \times 10^{12}\,M_\odot$ (e.g., A.-C. Eilers et al. 2024), in line with their stellar masses of $\gtrsim 10^{10}\,M_\odot$ (M. Yue et al. 2024b). The much higher number densities of BL-Hα emitters, on the other hand, suggest that they reside in less massive halos (E. Pizzati et al. 2025), in agreement with first clustering measurements using photometric and spectroscopic redshifts (J. Arita et al. 2025; X. Lin et al. 2025).

Here we present a new empirical approach to understand the host galaxies of BL-Hα emitters based on studies of their environments, in comparison to the large-scale environments of star-forming galaxies. We use BL-Hα emitters and neighboring galaxies identified in spectroscopic data from the "All the Little Things" (ALT) survey (see Section 2; R. P. Naidu et al. 2024). ALT is the deepest NIRCam grism survey undertaken to date and covers Hα emission at $z = 3.8$–5.0 down to star formation rates of $0.1\,M_\odot\,\mathrm{yr}^{-1}$. The NIRCam grism is ideal to map galaxy overdensities due to its simple line-flux-limited selection function over a wide field of view and the high precisions ($\approx 100\,\mathrm{km\,s}^{-1}$) of the redshifts (e.g., D. Kashino et al. 2023; F. Wang et al. 2023; F. Sun et al. 2024; T. Herard-Demanche et al. 2025). The ALT field is covered by 27-band JWST NIRCam photometry (e.g., R. Bezanson et al. 2024; K. A. Suess et al. 2024), as well as photometric data from the Hubble Space Telescope (HST), which yields nearly model-limited characterization of the SEDs. Our key assumptions are that the SED fits of galaxies without broad Hα emission are very good and that the presence of broad Hα emission is not impacting the detectability of galaxies in their environments.

We present the data that we use in Section 2. In Section 3, we present our sample of BL-Hα emitters at $z = 4$–5, the AGN properties inferred from the Hα line profile, and the reference sample of star-forming galaxies. We measure the environments of BL-Hα emitters and the reference galaxies in Section 4. In Section 5, we investigate the relation between overdensity and stellar mass and use this to infer the stellar mass of BL-Hα emitters. In Section 6 we investigate whether the overdensity depends on BH mass. We discuss the implications of our results in Section 7 and summarize our results in Section 8.

Throughout the paper we assume a standard flat ΛCDM cosmology (Planck Collaboration et al. 2020). Magnitudes are reported in the AB system.

2. Data

The main aim of this paper is to study the environments of a well-defined sample of broad-line Hα emitters at $z \sim 5$ and compare them to the environments of star-forming galaxies with excellent stellar mass measurements. Given the possibility that

BL-Hα emitters are hosted by galaxies with masses as low as $\approx 10^8 M_\odot$ (e.g., F. Pacucci et al. 2023), we require a very deep survey that includes large numbers of such low-mass galaxies. To achieve this, we use galaxies and AGNs identified in the Cycle 2 JWST/NIRCam Wide Field Slitless Spectroscopic survey "ALT" (PID 3516; PIs Matthee & Naidu). ALT is the deepest NIRCam grism survey undertaken to date, yielding a sample of ≈1600 galaxies with spectroscopic redshifts at $z \sim 0.3$–8.5 (R. P. Naidu et al. 2024), with a redshift error of $\approx 100\,\mathrm{km\,s^{-1}}$ (R. Bordoloi et al. 2024; A. Torralba-Torregrosa et al. 2024). ALT targets galaxies in the $\approx 30\,\mathrm{arcmin^2}$ region in the background of the powerful lensing cluster A2744, building on the legacy from earlier surveys with HST and JWST, primarily the NIRCam imaging from the UNCOVER project (R. Bezanson et al. 2024), but see R. P. Naidu et al. (2024) for a full list of programs that contributed data. Additionally, the Cycle 2 medium-band program MegaScience (K. A. Suess et al. 2024) further completed the NIRCam medium-band coverage, yielding optimal characterization of galaxy SEDs with 27 bands. The spectroscopic galaxy sample was constructed by identifying emission lines in two-dimensional grism spectra with a criterion for the signal-to-noise ratio (S/N) of >5. The typical 5σ line-flux sensitivity ranges from $(6 \text{ to } 20) \times 10^{-19}\,\mathrm{erg\,s^{-1}\,cm^{-2}}$ at 3.15–3.95 μm. The identification of the lines used the detection of multiple emission lines (such as the [O III] doublet or He I + Paschen-γ) and/or photometric data. The median magnification of the sample is relatively modest, $\mu = 1.83$, and 83% of the sample has a magnification $\mu < 3$. Compared to the full galaxy catalog with photometric redshifts, we find that ≈60% (30%) of the galaxies with F444W < 26 (28) between $z = 4$ and 5 have a spectroscopic redshift from ALT, highlighting the high completeness of the sample. For full details of the survey design, data reduction, and galaxy selection we refer to the survey paper (R. P. Naidu et al. 2024).

3. Sample

3.1. AGN Sample

In the ALT data, Hα is covered at $z = 4$–5, which is therefore our prime redshift of interest. Broad Hβ lines could be found to higher redshifts (e.g., V. Kokorev et al. 2023); however, in broad-line AGN identified with JWST, the broad component of the Hβ line typically is more than three times fainter than that of the Hα line (M. Brooks et al. 2025). Further, our environment measurements cover a smaller dynamic range at $z \sim 6$, simply because there are fewer massive galaxies at earlier times due to the buildup of the galaxy stellar mass function.

We select broad Hα line emitters primarily based on their line emission in the ALT data by inspecting all 628 Hα emitters in the $z = 3.8$–5.05 range. Following the methods outlined by J. Matthee et al. (2024), we optimize the continuum subtraction of their grism spectra by explicitly masking a large region around the Hα line when estimating the continuum level, in order to prevent oversubtraction of broad components, and then fit the Hα + [N II] complex with a combination of a narrow Gaussian component and a broad one.

Six broad Hα line emitters are identified at $z = 3.99$–5.05 with a robust detection (S/N > 5) of a broad component with $v_{\mathrm{FWHM}} > 1000\,\mathrm{km\,s^{-1}}$. In these objects, goodness-of-fit statistics such as reduced χ^2 and Bayesian information criterion (BIC) improve for two-component (narrow + broad) line profiles as compared to a single component (where we use $\Delta\mathrm{BIC} = \mathrm{BIC_{old}} - \mathrm{BIC_{new}} > 10$ as a criterion; see Table 4). Figure 1 shows the fitted Hα line profiles of 5/6 BL-Hα emitters in our sample. The Hα profile of the luminous ALT-66543 has been presented by I. Labbe et al. (2024). We also show false-color NIRCam images that illustrate their compact, red appearance.[21] Three of the six broad Hα line emitters have been identified already by J. E. Greene et al. (2024). ALT-16986 was selected by I. Labbe et al. (2025), but not yet followed up. The other two were not in their color-selected parent sample, suggesting that not all BL-Hα emitters display the so-called V-shaped spectrum, with a blue UV and a red optical continuum. Indeed, these are somewhat less red in the optical continuum (69688), or are relatively red in the UV (11345 with $\beta = -1.3$). No previously known broad Hα emitter in our coverage has been missed by our selection.

After correcting for magnification, we find broad Hα line luminosities ranging from $(4.3 \text{ to } 1700) \times 10^{41}\,\mathrm{erg\,s^{-1}}$, with a median of $10^{42}\,\mathrm{erg\,s^{-1}}$, with line-widths 1240–4540 $\mathrm{km\,s^{-1}}$ (median 1520 $\mathrm{km\,s^{-1}}$). Assuming that the BLs originate from AGN activity (see, e.g., J. Matthee et al. 2024 for detailed arguments backing the AGN assumption, and also Section 7.1), we infer the SMBH mass and the bolometric luminosity from the Hα line properties, following A. E. Reines et al. (2013) and A. E. Reines & M. Volonteri (2015) for the mass and J. E. Greene & L. C. Ho (2005) and G. T. Richards et al. (2006) for the luminosity, assuming no attenuation corrections that could lead to a higher BH mass. The basic properties of our sample of broad-line Hα emitters are listed in Table 1.

In Figure 2, we show a compilation of broad Hα line luminosities and line widths at $z = 4$–5 from various surveys. The NIRCam grism surveys include ASPIRE (X. Lin et al. 2024), EIGER, FRESCO (J. Matthee et al. 2024), and ALT (this paper). The NIRSpec surveys include JADES (R. Maiolino et al. 2024a), a combination of the CEERS (which was included by, e.g., Y. Harikane et al. 2023 and D. D. Kocevski et al. 2023b) and RUBIES (A. de Graaff et al. 2025a) surveys presented by A. J. Taylor et al. (2025), and the UNCOVER program (J. E. Greene et al. 2024). Due to the depth of the ALT data compared to shallower grism surveys and the lensing magnification, the majority of the BL-Hα emitters in the ALT data probe the faint end of the sample, overlapping with the faintest samples from JADES, UNCOVER, and CEERS obtained through NIRSpec spectroscopy. Figure 2 also highlights how unrepresentative the luminous ALT-66543 (I. Labbe et al. 2024) is of the overall BL-Hα sample, explaining why we exclude it from calculations of sample averages in this paper.

We used PROSPECTOR to fit the SEDs of all emission-line galaxies in the ALT survey with stellar population models that self-consistently include the nebular emission from the fitted stellar populations, as detailed by R. P. Naidu et al. (2024). All JWST photometry is used in these fits, excluding filters that include flux below 1240 Å such that the fit is not impacted by variations in the Lyα emission line or the transmission of the intergalactic medium bluewards of the Lyα break. The emission-line fluxes measured from the grism data are not used in the fitting, but we note that various strong emission

---

[21] The spectrum of the exceptionally luminous object ALT-66543 has such a high signal-to-noise ratio that we fit the broad component with a Lorentzian wing (see I. Labbe et al. 2024 for details and also a discussion of the detection of Hα absorption in its spectrum).

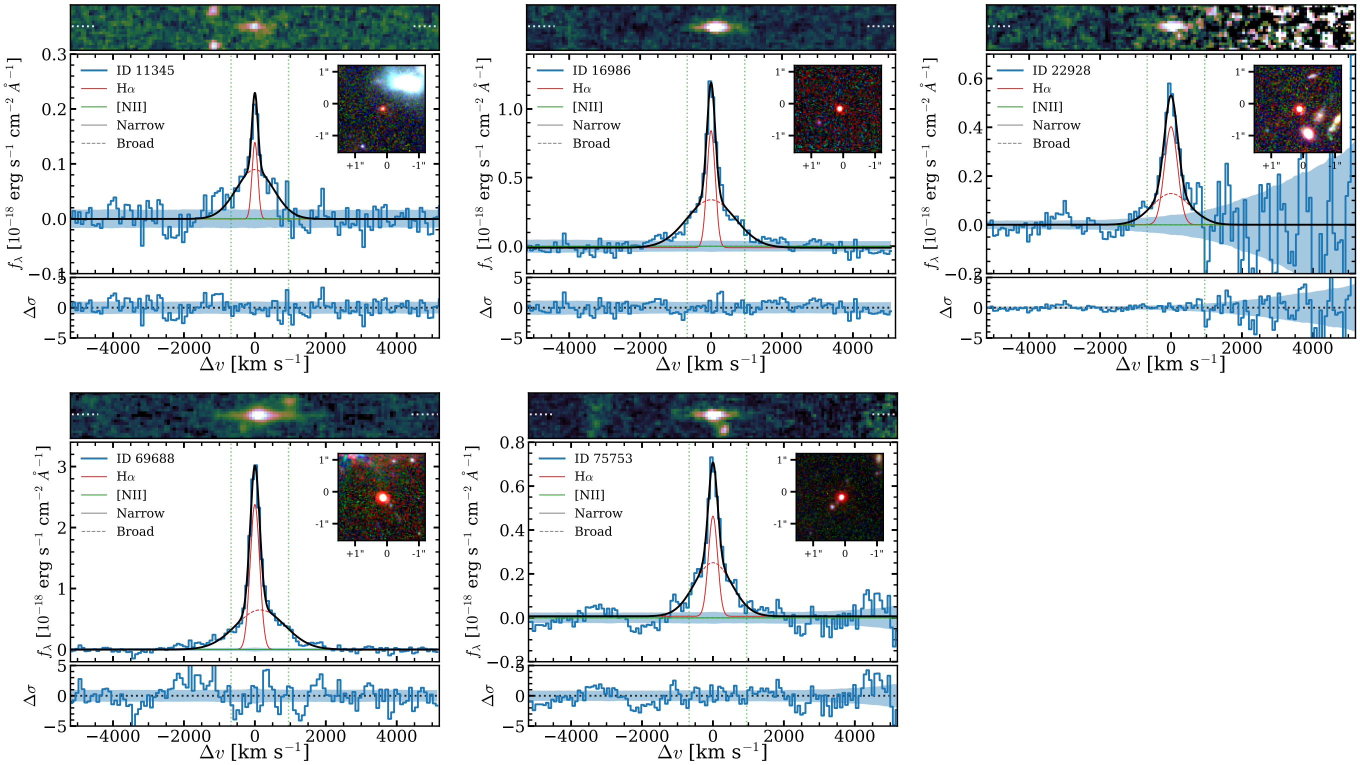

Figure 1. The Hα profiles of the main sample of BL-Hα emitters studied in this paper measured in the NIRCam grism data. Top panels show the 2D continuum-subtracted grism spectra. The middle panels show the optimally extracted 1D spectra. Blue lines show the data, where shaded regions show the errors. The black line shows the combined fit that is composed of a narrow Hα line and a broad one and narrow [N II]. The red dashed and solid components show the broad and narrow Hα components and green shows the best-fit [N II] line, whose wavelength we highlight with dotted green lines. The bottom panels shows the residuals of the spectral fit. Inset panels show false-color rest-frame optical RGB images constructed from NIRCam F115W/F200W/F356W images, highlighting the point-source morphology of the objects.

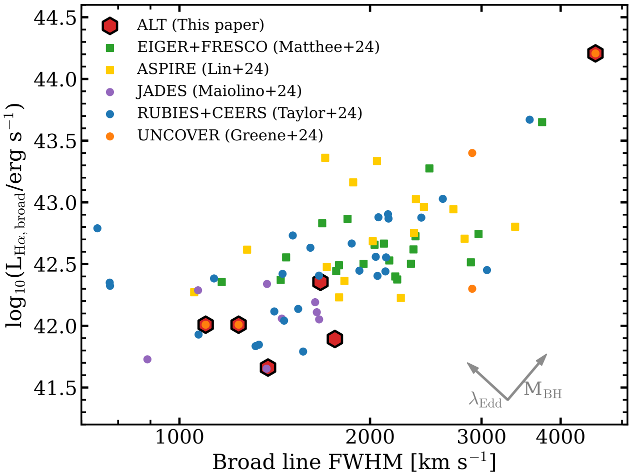

Figure 2. Compilation of Hα broad lines measured with JWST at $z = 4$–6 from NIRCam Grism (red hexagons, this paper; green squares, EIGER and FRESCO; yellow squares, ASPIRE) and NIRSpec (points: purple, JADES; blue, RUBIES and CEERS; orange, UNCOVER) spectroscopy. We highlight how the Hα luminosity and width change with SMBH mass and Eddington ratio under the commonly adopted calibrations used. Three of the ALT sources are also in the UNCOVER sample.

lines typically strongly boost the photometry in filters with bandwidths. Importantly, for almost all sources the available photometry also covers the optical continuum, free from emission-line contamination.

In Figure 3, we show the SEDs of the BL-Hα emitters inferred from photometry. We stress that the SED fits for the BL-Hα emitters are displayed primarily for illustrative purposes, as no AGN component is included in the fits. Generally, the PROSPECTOR models are flexible enough to yield reasonable fits to the data, with relatively high stellar masses $M_{\rm star} = 10^{7.7-10} M_\odot$. However, as discussed in detail by for example B. Wang et al. (2024), the inclusion of a red AGN component could lead to drastically lower stellar masses (i.e., by ∼1 dex). Inspecting the SEDs in Figure 3 in detail, we remark somewhat poorer performance around the Balmer break region (observed wavelength ≈2–2.5 μm for most sources), in particular in ALT-22928, ALT-69688, and ALT-75753. Comparing the derived properties to the main galaxy sample at $z \sim 4$–5, we notice that the BL-Hα emitters unusually combine a high inferred stellar mass with a young age. These fitted parameters are primarily driven by the unusual combination of a Balmer continuum break with a blue UV continuum.

3.2. Galaxy Sample

In order to accurately and uniformly map the environment of the BL-Hα emitters, we only use galaxies in our highly complete sample with spectroscopic redshifts and with a conservative line luminosity threshold that effectively yields a volume-limited sample. The inclusion of galaxies that only have a photometric redshift could increase our galaxy pair count statistics, but at the expense of more noise and (more importantly) a selection function that is challenging to quantify. Moreover, it would not increase our BL-Hα sample, whose size is more limiting. While the photometric redshifts in our survey field are generally very accurate, this is not always

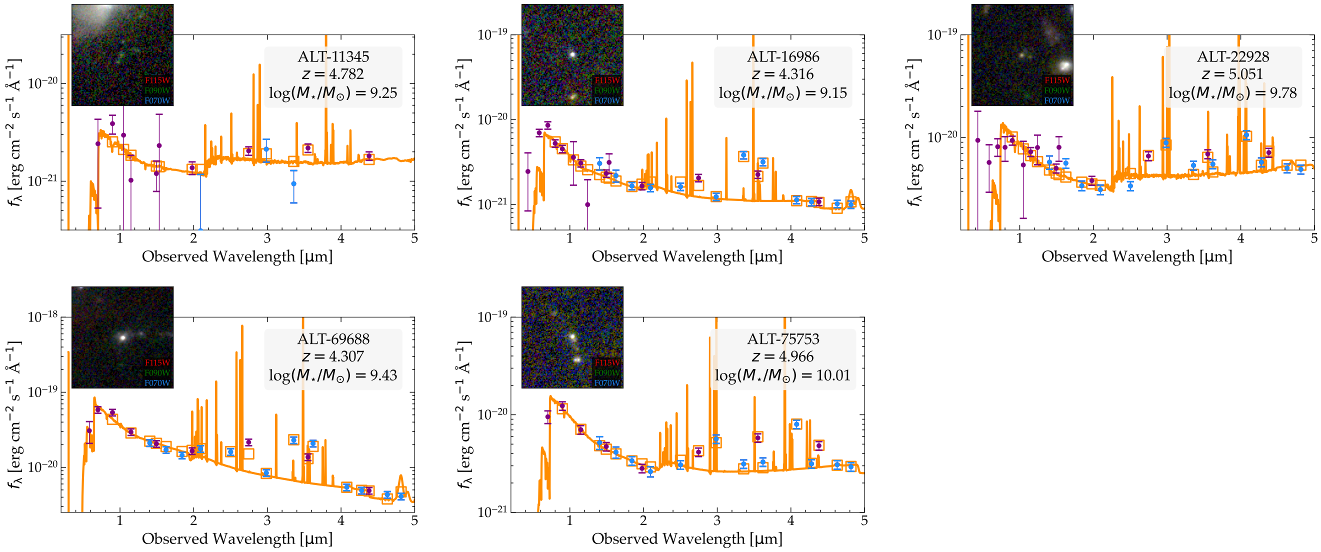

Figure 3. SED fits of the five BL-Hα emitters that are the main focus of this paper. Orange curves and shaded regions show the best-fit SEDs *assuming pure stellar and nebular emission* and their uncertainties that ignore an AGN contribution. Purple data points are measurements in broadband filters, while blue data points are medium-band filters. Inset stamps are false-color rest-frame UV RGB images of 2.″4 × 2.″4 based on the F070W, F090W, and F115W NIRCam imaging data.

Table 1
General Properties of the Broad-line Hα Emitters Used in This Work

ALT-ID	R.A.	Decl.	$z_{\rm spec}$	μ	$v_{\rm FWHM}$ (km s^{-1})	$\log_{10}(L_{\rm bol}/{\rm erg\ s^{-1}})$	$\log_{10}(M_{\rm BH}/M_\odot)$	$(1+\delta)_{1\ \rm cMpc}$
11345	3.570070	−30.432089	4.782	1.50 ± 0.30	1380 ± 220	44.1 ± 0.2	$6.7^{+0.2}_{-0.2}$	4.0 ± 1.7
16986	3.598798	−30.418733	4.316	2.69 ± 0.54	1760 ± 290	44.3 ± 0.2	$7.1^{+0.2}_{-0.3}$	7.4 ± 3.6
22928*	3.550840	−30.406599	5.051	1.61 ± 0.32	1100 ± 110	44.4 ± 0.2	$6.7^{+0.2}_{-0.2}$	6.3 ± 3.0
66543*	3.584759	−30.343629	4.464	1.81 ± 0.36	4540 ± 50	46.3 ± 0.2	8.8 ± 0.2	30.9 ± 5.4
69688	3.569437	−30.348231	4.307	2.08 ± 0.42	1670 ± 50	44.7 ± 0.2	7.2 ± 0.2	10.1 ± 5.2
75753*	3.530008	−30.358013	4.966	2.24 ± 0.44	1240 ± 90	44.4 ± 0.2	6.6 ± 0.2	4.3 ± 2.5

Note. Coordinates are in the J2000 reference frame. Objects with a * have already been identified by J. E. Greene et al. (2024; ALT-22928 = G23-10686; ALT-66543 = G23-45924; ALT-75753 = G23-38108). We list the line width ($v_{\rm FWHM}$) of the broad Hα component, the bolometric luminosity derived from the Hα line, and the BH mass. We also list the overdensity within a radius of 1 cMpc around the BL-Hα emitters measured in this work. Errors on magnifications are dominated by systematics that we estimate to be at the 20% level.

true for specific redshifts (see Section 5.5 of R. P. Naidu et al. 2024 for a detailed discussion), as the accuracy of photometric redshifts may depend significantly on the accuracy of the (wings of the) filter transmission curves and on the properties of galaxies. Any redshift error could propagate strongly in the measured redshift difference between galaxy pairs and dilute the clustering signal. Therefore, we focus on spectroscopically selected samples, as is commonly done in high-redshift clustering studies (e.g., F. Wang et al. 2023; A.-C. Eilers et al. 2024; E. Pizzati et al. 2024; X. Lin et al. 2025; M. Shuntov et al. 2025b). We impose a limiting Hα luminosity of 2×10^{41} erg s^{-1}, which corresponds to a typical S/N > 10 and an unobscured star formation rate threshold of $\gtrsim 0.6\,M_\odot$ yr^{-1} (see C. Di Cesare et al. 2025, in preparation). Note that using a fixed luminosity threshold, rather than a flux threshold, also balances the wavelength-dependent sensitivity (which is somewhat better at longer wavelengths). We also ignore any region with a magnification $\mu > 3$ such that our on-sky distributions are not strongly impacted by differential volumes due to changes in magnifications (we have verified that changing limits from $\mu = 2$ to $\mu = 4$ does not impact the results we obtained). As a consequence, our final galaxy sample that we use to measure the environment consists of 308 galaxies with redshifts $z = 3.8$–5.05.

Based on the PROSPECTOR fits to the photometry, we find that the typical galaxy in our sample has a mass of $10^8\,M_\odot$ (ranging from 5×10^6 to $2 \times 10^{10}\,M_\odot$), a UV luminosity $M_{\rm UV} = -18.8$ (ranging from −14.5 to −21.5) and an unobscured star formation rate ${\rm SFR}_{\rm H\alpha} = 1.4\,M_\odot$ yr^{-1} (ranging from 0.6 to 24 $M_\odot$ yr^{-1}). In Figure 4, we show example SED fits of galaxies in our sample, with stellar masses of 10^7, $10^{8.5}$, and $10^{10}\,M_\odot$, from top to bottom. The models are very tightly constrained thanks to the spectroscopic redshift and the large number of filters, implying that stellar mass uncertainties are limited by systematics. We also note that the SED of ALT-71962, a normal galaxy with narrow Hα emission and with a similar fitted mass to some BL-Hα emitters, is characterized by a relatively old stellar population, with a red UV slope.

3.3. The Colors of Normal and Broad Hα Line Emitters

Figure 5 shows the distribution of the F150W − F444W colors from the galaxy sample versus the (magnification-corrected) F444W magnitude, where galaxies are colored by their stellar mass. We chose to use observed magnitudes and colors for a model-independent comparison between the galaxies and the BL-Hα emitters. At $z = 4$–5, the F150W and F444W photometry is not sensitive to strong emission lines and probes the difference in the continuum level from

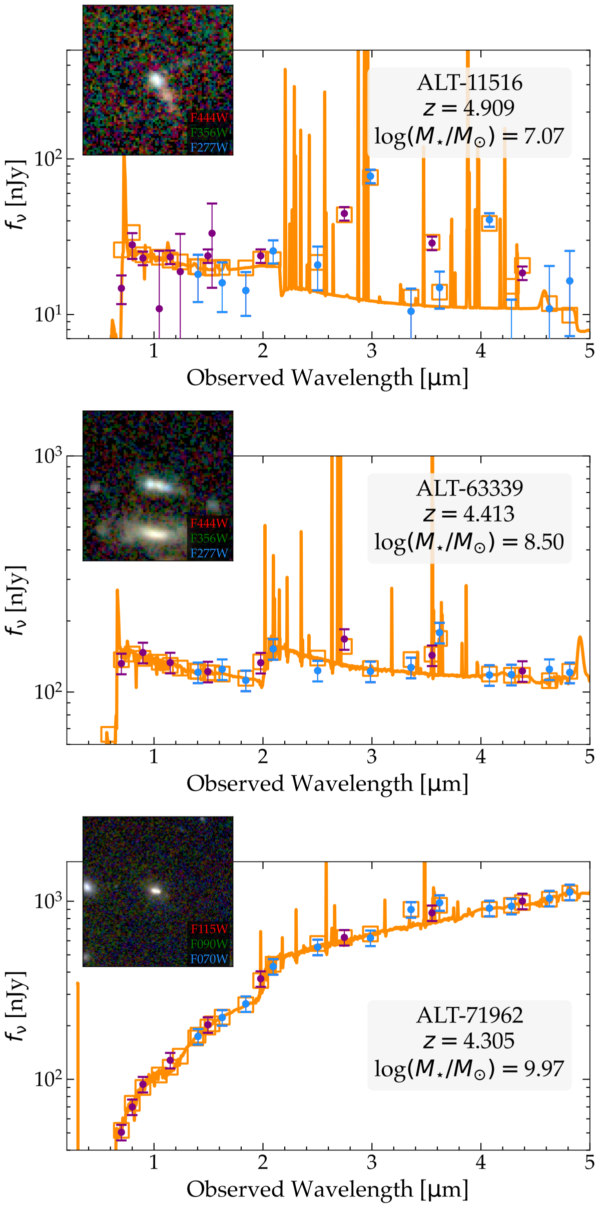

Figure 4. Example SED fits of galaxies in the reference sample of galaxies without broad Hα lines in the ALT data. The masses increase from top to bottom—10^7, $10^{8.5}$, and 10^{10} $M_\odot$. Orange curves and shaded regions show the best fits and their uncertainties. Purple data points are measurements in broadband filters, while blue data points are medium-band filters. Inset stamps are false-color RGB images of 3″ × 3″ based on the F070W, F090W, and F115W NIRCam imaging data, revealing the diverse and resolved morphologies of these galaxies.

rest-frame wavelengths $\lambda_0 = 0.27$–$0.8\ \mu$m, and thus captures the Balmer discontinuity that is of particular interest (e.g., D. J. Setton et al. 2024a; B. Wang et al. 2024).

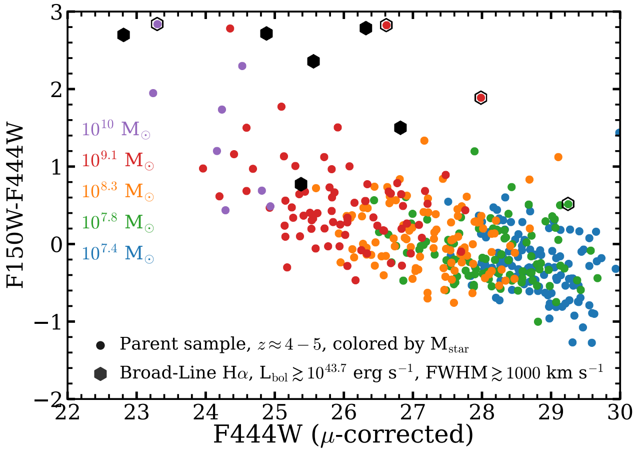

Figure 5. The observed F150W − F444W colors vs. the (magnification-corrected) F444W magnitude of our galaxy (points colored by their stellar mass) and broad-line Hα samples (black hexagons). The F150W − F444W colors probe the difference in the continuum level from rest-frame wavelengths $\lambda_0 = 0.27$–$0.8\ \mu$m, free from emission-line contamination. Open hexagons show sources with suspected broad lines (based on the colors and morphology). The stellar masses of the sample correlate with the F444W magnitude and range from ≈2×10^7 $M_\odot$ (blue) to ≈10^{10} $M_\odot$ (purple).

Galaxies with a fainter F444W magnitude are generally less massive and they have flat or even blue F150W − F444W colors, the latter indicative of Balmer jumps (e.g., H. Katz et al. 2024). Massive galaxies tend to have redder F150W − F444W colors due to Balmer breaks, but few as red as the colors of the most luminous BL-Hα emitters. Generally, all BL-Hα emitters have red F150W − F444W colors, suggesting that the AGN activity is reddening the rest-frame optical colors. Four BL-Hα emitters have extremely red F150W − F444W colors (>2), which are particularly exceptional among the fainter magnitudes (F444W > 25). One of the BL-Hα emitters (69688) is significantly less red and has colors similar to galaxies without broad Hα lines. Object 69688 has a relatively strong narrow component on top of a significant broad component. This is in agreement with the sample presented by J. Matthee et al. (2024) that showed a correlation between optical redness and the fraction of total Halpha flux that is in the broad component. There are two galaxies with a relatively high mass given their faint F444W magnitude (F444W > 26; ALT IDs 16772 and 62404; coordinates and redshifts can be found in the public ALT catalog: R. Naidu & J. Matthee 2024). These have colors similar to the typical BL-Hα emitters, but our data are likely not sensitive enough to identify their broad Hα components. An interesting implication of these trends is that not all BL-Hα emitters have red UV to optical SEDs (e.g., ALT-69688), and they may thus be missed by V-shaped photometric selection criteria (see also K. N. Hainline et al. 2025 for similar results based on a detailed investigation of the impact of color selections on the completeness of AGN selections). We note that the luminous, red galaxy ALT-62975 is a possible AGN due to its compact yet resolved appearance. However, the Hα profile analysis is complicated by a nearby component such that two emission components are separated almost exactly in the direction of the (single available) dispersion angle, complicating the identification of a possible faint broad component, and exceptionally strong [N II] emission. We discuss the detailed properties of 62975, as well as the properties of other suspected BL-Hα emitters, in Appendix B.

4. The Environments of Galaxies and of Little Red Dots

4.1. Redshift Distribution

In Figure 6 we show the redshift distribution of the galaxy sample and we highlight the redshifts of the BL-Hα emitters. Most galaxies are found in about 10 redshift spikes, i.e., ≈50% of the galaxies are found within 10 regions of $\Delta z < 0.02$. The strongest overdensities are at redshifts $z \approx 3.8$, $z \approx 4.0$ (which is associated with the passive galaxy identified recently by D. J. Setton et al. (2024b), and the massive ALT galaxy ALT-62975 that we flag as a suspected AGN), $z \approx 4.3$, and

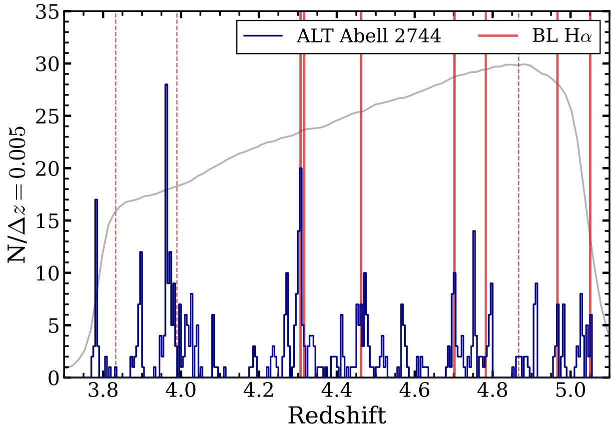

Figure 6. The redshift distribution of our galaxy and BL-Hα sample behind the A2744 lensing cluster. Red lines mark the redshifts of the BL-Hα emitters. Dashed lines show the redshifts of the tentative broad-line emitters discussed in the text and highlighted in Figure 5. The gray curve shows the F356W filter curve that was combined with the grism observations that we use.

$z \approx 4.7$. Besides spikes, there are also various notable underdensities, such as the one at $z \approx 4.1$. The most massive galaxies (without broad Hα emission) are at redshifts $z = 3.975$, 4.305, 4.296, 4.462, and $z = 4.272$, ordered by stellar mass. Each of these thus corresponds to a large redshift spike, with $\gtrsim$10 galaxies within 1500 km s^{-1}. This suggests that there is a strong correlation between the overdensity and stellar mass that we explore and utilize below. The BL-Hα emitters tend to be found in somewhat overdense regions, but none of them are found in the most overdense region in the field. This is also the case for the BL-Hα emitters identified in the FRESCO survey (P. A. Oesch et al. 2023; A. Covelo-Paz et al. 2025; J. M. Helton et al. 2024). Whether these results are simply because overdense regions have more galaxies, thus boosting the likelihood of catching a galaxy with broad-line AGN activity, or whether there is also relation between AGN activity and halo mass, will be explored in the next section.

4.2. The Projected Pair Count Distributions

In this section we characterize the environment of the BL-Hα emitters using the galaxy sample described above. We focus on the projected separations among galaxies in the plane of the sky. We compute source-plane positions based on the spectroscopic redshifts and the lens model from L. J. Furtak et al. (2023, updated as described by S. H. Price et al. 2025). We find that the distribution of velocity differences between all pairs of galaxies with separations (0, 2] arcmin has a very tight peak centered around $\Delta v = 0$ km s^{-1}, with an FWHM of 500 km s^{-1}. Therefore, we assume that galaxies with velocity differences $\Delta v < 1500$ km s^{-1} ($\Delta z/(1 + z) < 0.005$) are associated with each other. Our results are stable when this cut is changed from 500 to 3000 km s^{-1}. If redshift differences are purely due to the Hubble flow, then $\Delta v \approx 1500$ km s^{-1} corresponds to ≈3 cMpc at $z = 4.5$.

In Figure 7, we illustrate the environments of three of our BL-Hα emitters that display a range in overdensities. The environments of the others are shown in Appendix A. The right panels illustrate that the typical overdensities are confined within $\Delta v < 1000$ km s^{-1}, justifying our choice of associating galaxies in a redshift window as narrow as 1500 km s^{-1}. A range of environments can be seen among the BL-Hα emitters. ALT-11345 has a very typical environment with a few neighbors within a radius of 1 cMpc (which we use as a reference scale, but our results are robust to changes from 0.5 to 4 cMpc), while ALT-66543 and ALT-69688 both show several companions. Noteworthy is that ALT-69688 is at a redshift with a large overdensity, but the object itself is not in the spatial center of the overdensity (which instead is close to one of the most massive star-forming galaxies in our sample). The extremely luminous ALT-66543, on the other hand, appears in the center of an extreme overdensity—the largest on 1 cMpc scales in our full survey. Within this region, there are several other relatively massive galaxies, including one that has a stellar mass of $3 \times 10^9\, M_\odot$. Generally, these illustrations suggest that BL-Hα emitters sample a range in environments and do not appear strongly correlated with themselves.

We quantify the overdensity of each object by normalizing the number of neighbors within a cylinder with radius 1 cMpc and redshift difference $\Delta z/(1 + z) < 0.005$ to the random expected number counts, i.e., $1 + \delta_{<R} = N(<R)/\langle N(<R)\rangle$, where δ is the overdensity within radius R. At 1 cMpc, the two-halo clustering term dominates over the one-halo term in low-mass galaxies at high redshift such as Lyα emitters (e.g., Y. Herrero Alonso et al. 2023). The random expectation is empirically measured using the average of the number counts measured around a uniform grid of source-plane coordinates (R.A., decl., z), correcting for the fraction of the volume within radius R that is covered by our survey and has $\mu < 3$. At our reference scale of 1 cMpc, this number is 0.8 per $\Delta z/(1 + z) = 0.005$. Table 1 lists the overdensities for the BL-Hα emitters, which range from $1 + \delta = 1.2$ to 30.9, with a median of 5.3 ± 1.4 (mean 5.6 ± 1.2) when excluding ALT-66543, which has an exceptional luminosity and line width and is therefore not representative (Figure 2).

4.3. Comparison to Star-forming Galaxies

In order to interpret the overdensities measured around the BL-Hα emitters, we here perform an empirical comparison to overdensities measured around the other galaxies in our sample that do not show broad Hα line emission. The SEDs of these galaxies are well described with stellar population models (see Figure 4) and we can therefore infer their stellar masses, and subsequently investigate the relationship between stellar mass and overdensity factor. The main motivation for this approach is that this reference sample is subject to similar systematic effects in the overdensity measurements.

In Figure 8, we show the average number of galaxy pairs as a function of projected radius (in the source plane) within $\Delta z/(1 + z) < 0.005$, taking into account the effective area around each galaxy that is determined by our field of view and the area that has a magnification $\mu < 3$. Our average curve for BL-Hα emitters excludes ALT-66543, given its exceptional BH mass and luminosity that are more than an order of magnitude higher than all others in the sample (see Table 1 and Section 6). We also show the average pair counts around galaxies in bins of stellar mass. The first four stellar mass bins are chosen to have similar numbers of galaxies (≈60), whereas the highest stellar mass bin is chosen to have (at least) seven galaxies. We illustrate the uncertainty due to variation within the samples with the shaded regions, which show the 16th–84th percentiles of the pair counts when bootstrap resampling the subsets 1000 times (with replacement). These uncertainties are mostly important for small samples, i.e., the most massive galaxies and BL-Hα emitters. Compared to this random expectation, an excess number of pairs is detected at all radii for all masses. The measured slopes are also somewhat shallower

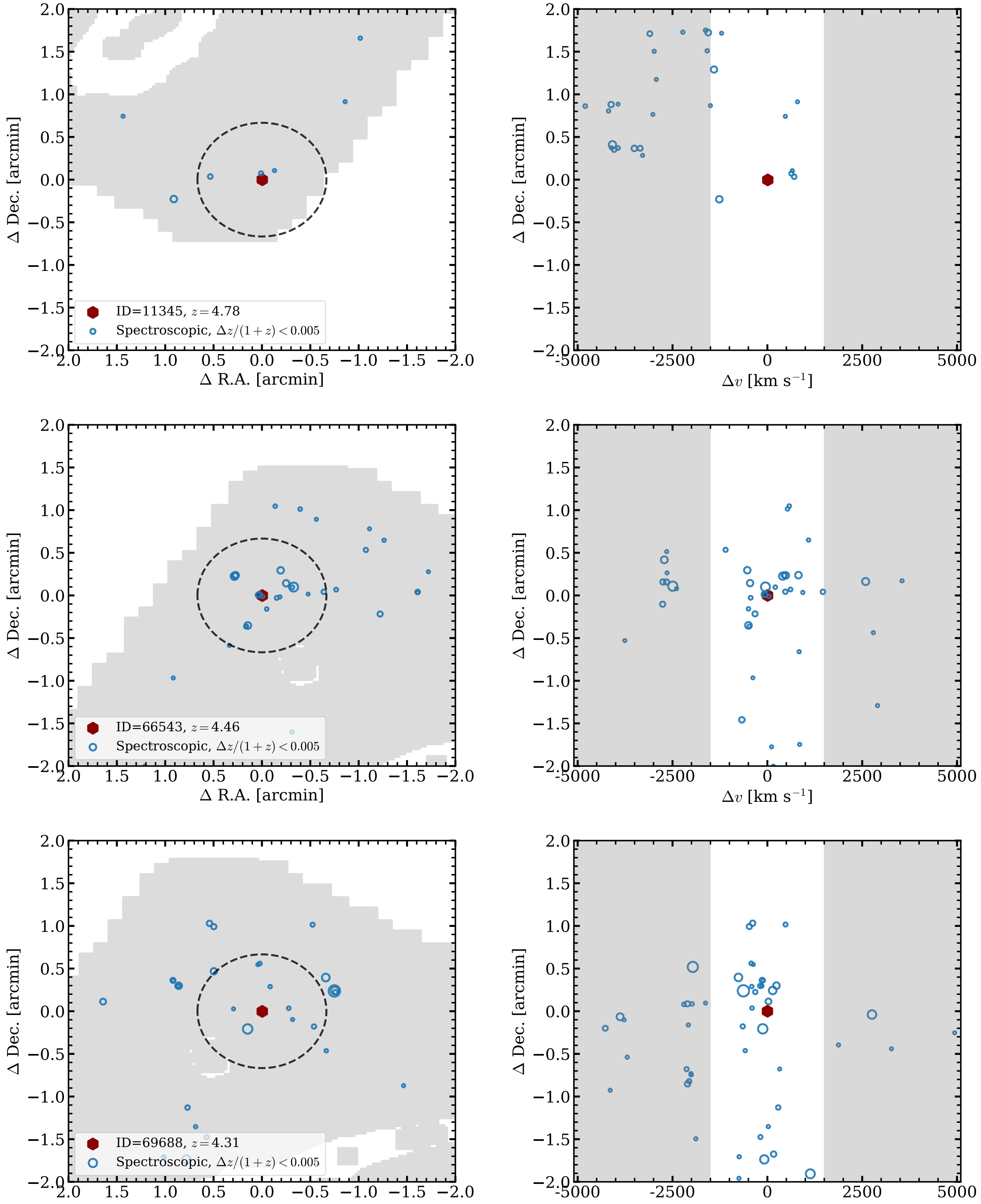

Figure 7. The environments of BL-Hα emitters (red hexagons), ordered from low density (top) to intermediate density (bottom). Left panels show the sky-plane distribution of the galaxy sample, where the gray region highlights the coverage (with $\mu < 3$). Blue circles are our spectroscopic galaxy sample (with a redshift difference $\Delta z/(1 + z) < 0.005$ to the BL-Hα emitter) and their size scales with stellar mass. The dashed circle roughly corresponds to a radius of 1 cMpc in the source plane. Right panels show the redshifts of the galaxies. Environments of the other BL-Hα emitters in our sample are shown in Appendix A.

than the random pair counts, indicative of a significant clustering signal (e.g., E. Pizzati et al. 2024). At large radii ($R > 50$ pkpc; $\gtrsim$0.25 cMpc), the average pair counts uniformly increase with stellar mass, showing that more massive galaxies are located in more overdense regions. This is expected when galaxy stellar mass is correlated with halo mass (e.g., M. Shuntov et al. 2022). The average pair counts around BL-Hα emitters suggest that their environments are similar to those of galaxies with stellar masses $\approx 10^8 \, M_\odot$. This is explored in more detail in Section 5.[22]

---

[22] We would find qualitatively similar results if we were to use galaxies with photometric redshifts to trace the environments, although the redshift uncertainties dilute the differences in clustering strengths as a function of mass.

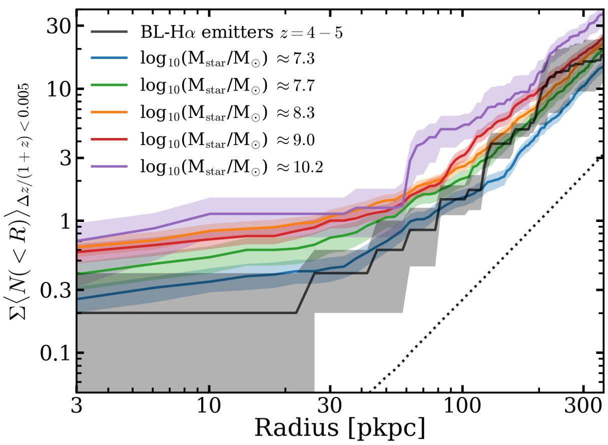

Figure 8. The average number of neighboring galaxies within a radius R and $\Delta z/(1 + z) < 0.005$ for BL-Hα emitters (black; excluding ALT-66543 due to its exceptional luminosity, see Figure 2) and for star-forming galaxies with various masses at $z \approx 4$–5 (colored lines). The dotted black line shows the expectation for random regions in our coverage. Shaded regions show the 16th–84th percentiles from bootstrap resampling the various subsets.

At radii below ∼100 pkpc, the pair counts are relatively flat (independent of radius), especially below 30 pkpc, yet they are still dependent on mass. This flat slope may not be surprising as these separations are in the one-halo regime, as the virial radius of a $\approx 10^{12(11)}\,M_{\odot}$ Navarro–Frenk–White halo is ≈60 (30) pkpc at $z \approx 4.5$. It appears that BL-Hα emitters typically are surrounded by a smaller number of neighbors, although the uncertainties are large due to the small-number statistics. In any case, these measurements do not suggest that BL-Hα emitters have an excessively large number of nearby pairs, as may be expected if their AGN activity were triggered by galaxy mergers (e.g., T. S. Tanaka et al. 2024).

4.4. Controlling for the Impact of Satellite Galaxies

The relatively flat pair counts within radii that roughly correspond to the virial radii of halos with masses $\approx 10^{11}\,M_{\odot}$ strongly suggest that we are identifying multiple galaxies belonging to the same halo. This could significantly impact studies of the larger-scale environment, in particular investigating a mass dependence. Low-mass satellite galaxies likely reside in a different environment than low-mass galaxies that are not satellites, as their large-scale environments are more biased (e.g., B. Diemer 2018; S. Ortega-Martinez et al. 2025). In order to investigate and control for this effect, we attempt to identify which galaxies are satellites and remove them when calculating the average pair count distributions as a function of stellar mass.

To develop an empirically motivated definition of a central–satellite distinction, we investigate the distribution of projected separations between galaxy pairs (with $\Delta z/(1 + z) < 0.005$). As can be clearly seen in Figure 9, the pair count distribution displays a minimum at around 2″–3″, and increases to both larger and smaller separations (similar to $z \sim 6$ galaxies; e.g., J. Matthee et al. 2023). Motivated by this, we define a satellite as a galaxy that has a more massive companion within a projected separation of 3″. This yields a satellite fraction ranging from about 30% at masses below $10^{8}\,M_{\odot}$ to 15% at $10^{9}\,M_{\odot}$, and virtually zero beyond that. Figure 9 illustrates that the pair count distribution around central galaxies (i.e., those that remain after removing satellites with this definition) drops at small separations, most prominently for low-mass galaxies.

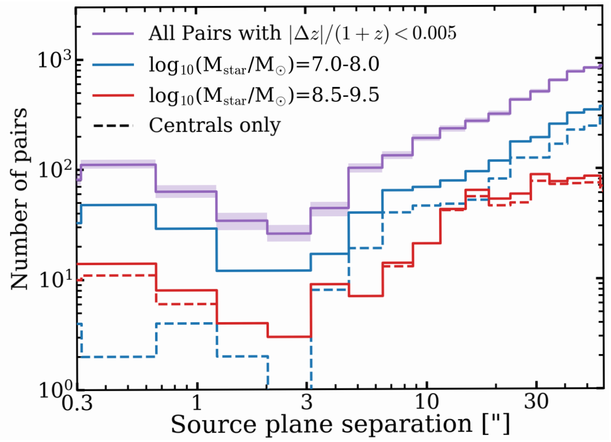

Figure 9. The distribution of the projected source-plane separations between pairs of galaxies (with $\Delta z/(1 + z) < 0.005$). Blue shows all pairs within our galaxy sample (where the shaded regions display the variation from bootstrap resamples). Blue and red solid lines show the distribution centering on galaxies with masses in the ranges $\log_{10}(M_{\rm star}/M_{\odot}) = 7.0$–8.0 and 8.5–9.5, respectively. Dashed lines show the distribution around "centrals" only, where a central is defined as a galaxy that has no companion within 3″ that is more massive than itself.

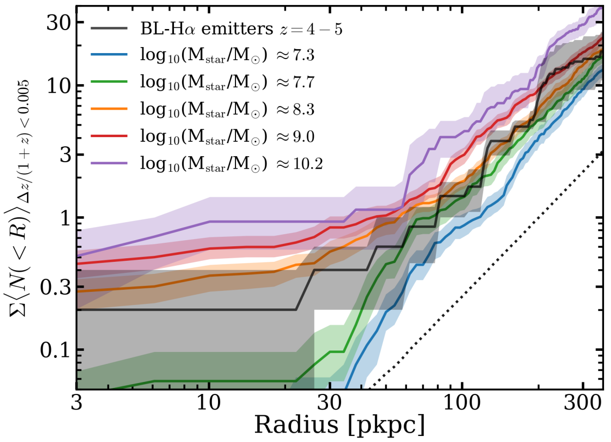

Figure 10. The average number of neighboring galaxies as a function of projected radius (as Figure 8), but now centering on centrals only. Here we implicitly assume that BL-Hα emitters are centrals.

Figure 10 shows the pair count distribution for galaxies that we identified as centrals. Compared to Figure 8, we identify an even clearer distinction between the average number of neighbors around galaxies with various masses, especially at smaller radii. This is because for low-mass galaxies, we now no longer include galaxies that are satellites to more massive galaxies (and which would therefore inherit their larger bias). With our sensitivity thresholds we detect one companion to ALT-75753 within 3″ (see Figure 1), which has a stellar mass of $2 \times 10^{7}\,M_{\odot}$, while we detect three companions to the luminous ALT-66543 with masses ranges from (6 to 40) $\times 10^{7}\,M_{\odot}$ (see also I. Labbe et al. 2024). The low stellar mass of the companions supports our assumption that BL-Hα emitters are typically centrals.

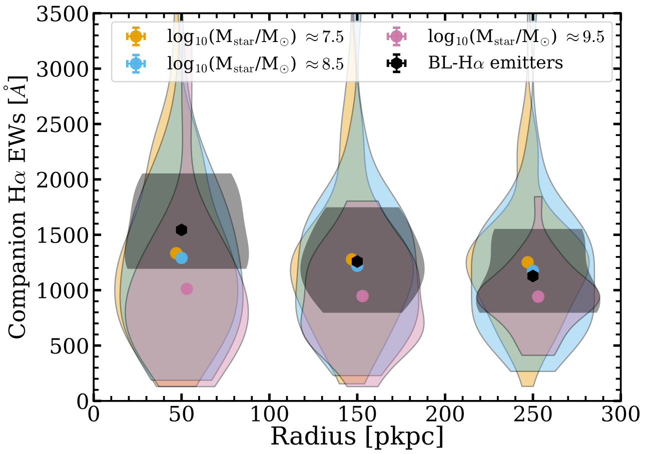

Figure 11. The distribution of rest-frame Hα EW of the companion galaxies as a function of projected radius around galaxies with masses $\approx 10^{7.5}$ $M_\odot$ (yellow), $\approx 10^{8.5}$ $M_\odot$ (blue), and $\approx 10^{9.5}$ $M_\odot$ (pink) and BL-Hα emitters (black), demonstrating that there is no significant bias due to the use of Hα. Violins are slightly shifted horizontally randomly for illustrative purposes.

4.5. Controlling for Biases Due to the Use of Hα as an Environment Tracer

To infer the physical properties of galaxies hosting broad Hα lines based on their large-scale environments, it is crucial to assume that our measurement of the large-scale environment is independent of the properties of the galaxies around which the environment is measured. This assumption could be invalid if the Hα emission-line selection were to lead to biased estimates of the overdensity, for example when the star formation rates in the large-scale environments around (passive) massive galaxies would systematically be lower (this is typically called galactic conformity), such that a selection limited by Hα line luminosity may primarily miss galaxies in such environments. Indications of galactic conformity at high redshift have recently been identified in protocluster environments at $z \approx 3$ that show a relatively high passive fraction (I. McConachie et al. 2025).

In order to check whether the properties of galaxies in the large-scale environments depend on stellar mass, or whether they systematically differ around BL-Hα emitters, we compare the Hα equivalent width (EW) distributions of the companion galaxies around galaxies as a function of mass or presence of BL-Hα, split by distance. These distributions are illustrated in Figure 11. We find that the companions around the most massive galaxies in our sample systematically tend to have somewhat lower EWs, although the variation among galaxies is large. A similar trend is seen if we use tracers of the Balmer break strength instead of Hα EW. These trends are a sign of galactic conformity, i.e., galaxies around the most massive galaxies are somewhat more evolved themselves as well (see also other evidence for accelerated evolution in overdense regions: R. P. Naidu et al. 2024; T. Morishita et al. 2025), leading to relatively lower Hα luminosities. Nevertheless, while the effect is relatively small, the typical EWs are also significantly higher than the lowest EWs in our sample (≈200 Å), suggesting that the possible underestimation of galaxy overdensities around massive galaxies is likely small.

On scales beyond 100 pkpc, the Hα EWs of galaxies around BL-Hα emitters are similar to those of the companion galaxies around galaxies with masses $\sim 10^{7.5-8.5}$ $M_\odot$, suggesting that the large-scale environments of BL-Hα emitters are not particularly biased compared to those of normal galaxies. There is an indication of a skew toward larger Hα EWs at smaller distances, which could be indicative of a slight excess of star formation activity in the nearby environment of BL-Hα emitters.

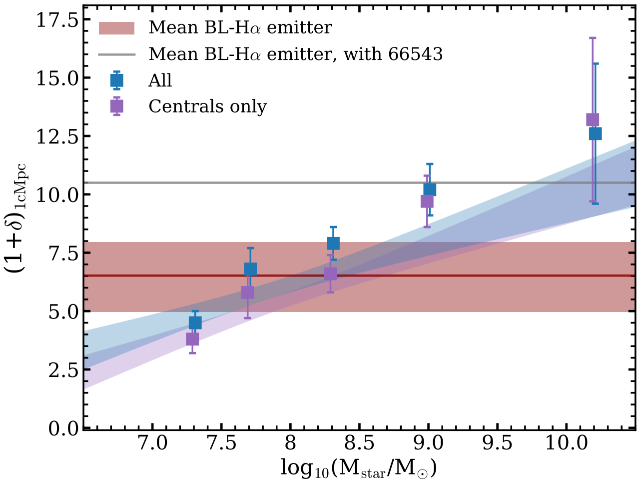

Figure 12. The relation between the overdensity (at a radius of 1 cMpc) and stellar mass of star-forming galaxies, either centering on all galaxies with a certain mass (blue) or on centrals only (purple). The red shaded region shows the mean overdensity around BL-Hα emitters, and its uncertainty based on bootstrapping, excluding ALT-66543. The gray line shows the mean when including ALT-66543.

Table 2
Overdensities as a Function of Stellar Mass

$\log_{10}(M_{\rm star}/M_\odot)$	$(1+\delta)_{\rm 1cMpc,All}$	$(1+\delta)_{\rm 1cMpc,Centrals}$
7.0–7.5 (7.3)	4.5 ± 0.6	3.8 ± 0.7
7.5–8.0 (7.7)	6.8 ± 0.9	5.8 ± 1.1
8.0–8.6 (8.3)	7.9 ± 0.7	6.6 ± 0.8
8.6–9.6 (9.0)	10.2 ± 1.1	9.7 ± 1.1
9.6–11.0 (10.2)	12.6 ± 3.0	13.2 ± 3.5

Note. We list the edges and average of the mass bins. Average overdensities around galaxies with these masses are calculated within 1 cMpc, both for all galaxies in that mass range and only for galaxies identified as central galaxies. Errors are estimated by bootstrapping the galaxy sample in each bin.

5. The Implied Host Galaxies of BL-Hα Emitters

Figure 12 shows that the overdensity measured on 1 cMpc scales strongly correlates with stellar mass. We illustrate results for a 1 cMpc radius as a reference, but note our results do not strongly depend on this choice. The measured overdensities are listed in Table 2. We also illustrate the mean overdensity around the BL-Hα emitters (excluding the exceptional ALT-66543) and its uncertainty, which is $1+\delta_{1\,\rm cMpc} = 6.5 \pm 1.4$. We fit a linear relation between overdensity and stellar mass:

$$1 + \delta_{\rm 1cMpc} = a + b\,\log_{10}(M_{\rm star}/10^9\,M_\odot), \quad (1)$$

For all galaxies, we find $a = 10.15 \pm 0.46$ and $b = 3.19 \pm 0.34$, while for central galaxies alone we find $a = 9.33 \pm 0.42$ and $b = 3.22 \pm 0.31$. When measuring overdensities on 2 cMpc scales, overdensities are generally slightly lower ($1+\delta_{2\,\rm cMpc} = 4.1 \pm 0.4$ for BL-Hα emitters), with a resulting $a = 8.04 \pm 0.40$ and $b = 1.9 \pm 0.31$ for all galaxies and $a = 7.63 \pm 0.37$ and $b = 2.11 \pm 0.30$ for centrals only. In all cases, a positive

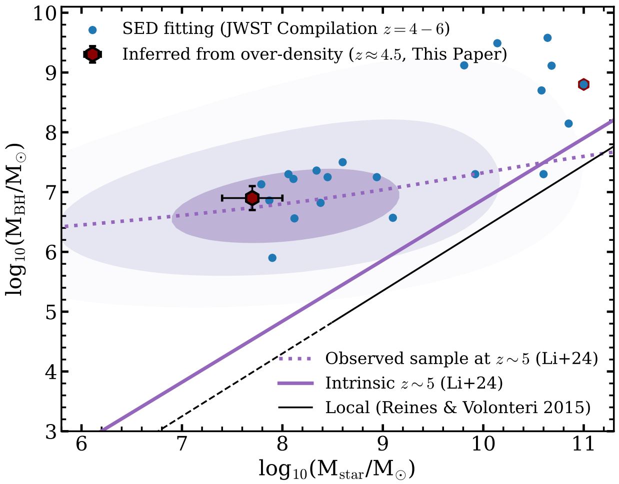

Figure 13. The relation between the stellar mass and SMBH mass for our BL-Hα emitter sample (dark red hexagon, where stellar mass is indirectly inferred from their environments), a JWST literature compilation at $z \approx 4$–6 (blue points, where stellar mass is inferred from SED fitting, from A. C. Carnall et al. 2023; Y. Harikane et al. 2023; V. Kokorev et al. 2024; R. Maiolino et al. 2024a; M. Onoue et al. 2024; M. Yue et al. 2024b). We highlight the luminous ALT-66543 (I. Labbe et al. 2024) also with a red hexagon. For reference, we show the local relation measured by A. E. Reines & M. Volonteri (2015) in black (and the extrapolated range marked by a dashed line). The luminosity-bias-corrected fit to JWST data from J. Li et al. (2025) is shown in purple; purple contours show the expected observed distribution from this modeling work.

correlation between stellar mass and overdensity is measured at $\gtrsim 6\sigma$ significance ($>10\sigma$ on 1 cMpc scales). We caution against extrapolating this relation toward higher overdensities as the relation may not be linear or changing, for example due to a flattening in the stellar to halo mass relation (e.g., M. Shuntov et al. 2025a). As discussed in Section 4.5, there is a slight indication that galaxies around the most massive galaxies have lower Hα EWs, such that we could possibly underestimate their overdensity, which could lead to a somewhat steeper relation, especially at the highest masses.

Using these correlations, we can infer the implied stellar masses of the galaxies hosting broad Hα lines, based on their overdensities. Here, we assume that BL-Hα emitters follow the same overdensity–stellar mass relation as galaxies without broad Hα. This method implies a stellar mass of $\log_{10}(M_{\rm star}/M_{\odot}) = 7.7 \pm 0.5$ (8.1 ± 0.5) when comparing the 1 cMpc overdensities for all (central) galaxies. At 2 cMpc, the implied masses would be $\log_{10}(M_{\rm star}/M_{\odot}) = 7.3 \pm 0.5$ (7.5 ± 0.4), respectively. Therefore, by averaging these masses, our indirect inference of the stellar mass based on their environments suggests that the typical BL-Hα emitter in our sample, which has a BH mass of $\log_{10}(M_{\rm BH}/M_{\odot}) = 6.9 \pm 0.2$, is hosted by a galaxy with a stellar mass of $\log_{10}(M_{\rm star}/M_{\odot}) = 7.7 \pm 0.3$.

In Figure 13, we compare our BH and stellar mass estimates with other estimates based on recent JWST measurements at $z = 4$–6 (combined from A. C. Carnall et al. 2023; Y. Harikane et al. 2023; V. Kokorev et al. 2024; R. Maiolino et al. 2024a). Similar to our work, BH masses are estimated from the single-epoch virial estimate using the broad Balmer lines (in most cases Hα). In these works, the stellar masses are estimated through SED fitting, using an image decomposition of point and extended sources (e.g., Y. Harikane et al. 2023; M. Yue et al. 2024b), including AGN model components (R. Maiolino et al. 2024a) or by fitting stellar absorption features to spectra (A. C. Carnall et al. 2023; V. Kokorev et al. 2024; M. Onoue et al. 2024). The mean stellar mass of our sample, which we indirectly inferred based on their environments, is in good agreement with these more direct methods, as well as recent results based on approaches that model the point-spread function (e.g., C.-H. Chen et al. 2025). The stellar mass is on average a factor 40 lower than the mass inferred from fitting galaxy-only SEDs (Figure 3). The typical stellar mass of $10^{7.7}$ $M_{\odot}$ suggests that these BL-Hα emitters have a high BH to stellar mass ratio of ≈12.5%. While this ratio is much higher than typically found for galaxies in the local Universe (e.g., F. Pacucci et al. 2023), we caution that this is partly due to biases resulting from the sensitivity limits at which broad Hα emission can be detected (e.g., H. Zhang et al. 2023; J. Li et al. 2025). Indeed, in Figure 13, we show the contour levels highlighting the expected distribution of an AGN sample with our Hα luminosity limit at $z \sim 4.5$ (J. Li et al. 2025), here assuming the galaxy stellar mass function of A. Weibel et al. (2024) and the intrinsic relation shown by the solid purple line.

It is interesting to compare our inferred stellar mass with the SEDs of the BL-Hα emitters (shown in Figure 3). Based on correlations between the optical colors, the compactness, and the broad Hα line profile, J. Matthee et al. (2024) argued that the AGN SEDs are (strongly) obscured and mainly outshine the host galaxy in the rest-frame optical, whereas the rest-frame UV emission is dominated by a (young) host galaxy (see also D. D. Kocevski et al. 2023b; M. Killi et al. 2024; H. B. Akins et al. 2025; Y. Ma et al. 2025). However, it is also possible that the rest-frame UV emission originates from a small fraction of scattered AGN light (e.g., J. E. Greene et al. 2024; M. Stepney et al. 2024), in particular as some BL-Hα emitters appear compact at virtually all wavelengths. We investigate the origin of the UV emission of the BL-Hα emitters by comparing their UV luminosity to the typical UV luminosity that is expected for a normal galaxy. Using the typical UV mass-to-light ratio in our reference sample, we find that their UV emission implies a stellar mass of $10^{7.7\pm0.2({\rm stat})\pm0.5({\rm sys})}$ $M_{\odot}$, where the statistical errors reflect the variation among UV luminosities of the BL-Hα emitters and the systematic errors reflects the variation in mass-to-light ratios of the reference sample. The similarity in the stellar masses inferred from large-scale environments and the UV emission suggests that the UV emission of these BL-Hα emitters indeed mainly originates from the star-forming host galaxy. This is in line with their very blue UV slopes, $\beta \approx -2$, which is bluer than typical quasars (see the compilation by, e.g., S. Fujimoto et al. 2022). In the rest-frame optical (i.e., $\lambda_0 = 0.6$–0.8 μm), the typical mass-to-light ratio would imply that BL-Hα emitters have much higher stellar masses of $\approx 10^{9.3}$ $M_{\odot}$, indicating a significant AGN contribution to the light.

6. The Variation among High-z AGN Environments

As illustrated in Figure 13, current samples of AGNs discovered and observed by JWST span three orders of magnitude in BH mass. This implies that we can expect similar variations in their host galaxies. Indeed, detailed fitting of the spectra and photometry of AGNs with SMBHs as massive as $\sim 10^{9}$ $M_{\odot}$ (e.g., X. Ding et al. 2023; I. Juodžbalis et al. 2024b; M. A. Marshall et al. 2024; M. Onoue et al. 2024; M. Yue et al. 2024b; B. Wang et al. 2025) suggests that their host galaxies are also significantly more massive ($M_{\rm star} \sim 10^{10-11}$ $M_{\odot}$) than those around lower-mass AGNs. In our analysis, we have excluded ALT-66543 from our sample averages due to its

Table 3
The AGN and Overdensity Measurements for a Compilation of High-redshift AGNs

ID	$z_{\rm spec}$	μ	$v_{\rm FWHM}$ (km s^{-1})	$\log_{10}(M_{\rm BH}/M_\odot)$	$\log_{10}(L_{\rm bol}/{\rm erg\ s^{-1}})$	$(1+\delta)_{1\ \rm cMpc}$	Survey
G23-13821	6.34	1.62 ± 0.32	3100 ± 710	8.1 ± 0.2	45.4 ± 0.2	23.8 ± 9.5	UNCOVER+ALT
G23-41225	6.77	1.88 ± 0.38	2000 ± 600	7.7 ± 0.4	45.3 ± 0.5	<9.5	UNCOVER+ALT
J0100+2802	6.33	1	6045 ± 20	10.06	47.18	54 ± 27	EIGER
J0148+0600	5.98	1	7828 ± 106	9.89	46.39	106 ± 38	EIGER
J1030+0524	6.30	1	3670 ± 15	9.19	46.30	<25	EIGER
J1148+5251	6.42	1	5370 ± 80	9.64	46.54	12 ± 12	EIGER
J159-02	6.38	1	3493 ± 30	9.10	46.20	<26	EIGER
J1148+5253	5.69	1	2910 ± 450	8.3 ± 0.1	45.8 ± 0.1	14 ± 14	EIGER

Note. For the UV-luminous quasars, EIGER measured their Hβ line width and derived the BH properties as detailed by M. Yue et al. (2024a). The bolometric luminosity is derived from L_{5100}. The errors on the BH mass and bolometric luminosity of the EIGER quasars are dominated by systematic errors. The BH properties of the $z\sim6$ LRDs from the UNCOVER survey are derived from the Hα line as detailed by J. E. Greene et al. (2024). G23-13821 corresponds to ALT-26902 and G23-41225 to ALT-73104. We measure the AGN properties of J1148+5253 based on its Hβ line in the EIGER data. Overdensities within 1 cMpc are measured in this paper. Upper limits are at the 2σ level.

much higher luminosity and BH mass. Its deep spectrum suggests a much higher stellar mass $\sim10^{11}\ M_\odot$ as well as AGN emission (I. Labbe et al. 2024). This is consistent with its very large overdensity $1+\delta\approx30$ (Table 1), which is significantly higher than the typical overdensity we measure for normal galaxies with masses $2\times10^{10}\ M_\odot$, $1+\delta\approx13$ (Table 2). Therefore, there is substantial evidence that there is significant variation among the host galaxies of high-redshift AGNs that may correlate with the BH mass.

We now directly investigate the relation between SMBH mass and the environment. Early clustering studies of BL-Hα emitters and the comparison of their number densities to those of quasars suggest that BL-Hα emitters reside in lower-mass halos than quasars (J. Arita et al. 2025; E. Pizzati et al. 2025). Here, we try to connect measurements of galaxy overdensity in these different samples directly by extending our dynamic range. First we add two BL-selected AGN at $z\sim6.5$ whose AGN properties are based on NIRSpec spectroscopy (J. E. Greene et al. 2024). G23-13821 at $z=6.34$ has a relatively high BH mass of $10^{8.1\pm0.2}\ M_\odot$, while G23-41225's BH mass appears lower ($10^{7.7\pm0.4}\ M_\odot$). We use the ALT data to measure their environments, similar to the methodology detailed in Section 4. Here, we use [O III] emitters as a probe of their environment rather than Hα-selected sources. These two populations of emission-line galaxies should similarly trace the large-scale structure, although [O III] emission is slightly more impacted by dust attenuation and is—unlike Hα emission—subject to variations in gas metallicity and ionization parameter. However, overdensities are measured with respect to the expected number of emission-line galaxies in random regions of the sky, controlling for such effects that could cause incompleteness. As above, we only include galaxies with $\mu<3$ and with a luminosity threshold of $L_{\rm [OIII]5008}>1.5\times10^{41}\ {\rm erg\ s^{-1}}$. We detect four galaxies within a radius of 1 cMpc and $\Delta z/(1+z)<0.005$ around G23-13821, but none around G23-41225, despite similar coverage and sensitivity. We measure overdensities on 1 cMpc scales of $1+\delta=23.8\pm9.5$ and $1+\delta<9.5$ (at 2σ), respectively, where errors are Poissonian. On 2 cMpc scales, their overdensities are 58.7 ± 8.2 and 7.6 ± 7.6. These measurements are listed in Table 3. We note that these overdensities are similar to those measured around a $z\sim7$ broad-line AGN by J.-T. Schindler et al. (2024) that has comparable Hβ-based AGN properties to these two sources.

Second, we add overdensity measurements around five UV-luminous quasars at $z=6.0$–6.4 measured using data from the EIGER survey (D. Kashino et al. 2023), see R. Mackenzie et al. (2025, in preparation). The quasar properties are based on NIRCam grism spectra (M. Yue et al. 2024b). The statistical errors are very low due to the very high signal-to-noise ratio of the spectra; thus, in Figure 14 we show the 0.3 dex systematic errors for their BH mass. We also add the X-ray-detected AGN J1148+5253 at $z=5.69$ (A. Mahabal et al. 2005). which is covered by the EIGER survey. We derive its AGN properties by fitting the Hβ and [O III] complex similar to the method detailed by M. Yue et al. (2024b), which yields a BH mass of $M_{\rm BH}=10^{8.3\pm0.1}\ M_\odot$. To measure the overdensity around these quasars, we use the same method as A.-C. Eilers et al. (2024), thus only including galaxies with [O III]$_{5008}$ luminosities above $10^{42}\ {\rm erg\ s^{-1}}$. The full details of the identification of [O III] emitters in the EIGER data will be presented by D. Kashino et al. (2025), but see also D. Kashino et al. (2023). Apart from variations in the sensitivity and the lack of cluster lensing magnification, the EIGER and ALT methodologies are very similar. The limited photometric coverage of the EIGER fields hampers our ability to check whether galaxy properties systematically vary around quasars (as in Section 4.5), but we note that we find no significant variations in UV luminosity, UV slope, [O III]/Hβ ratio or [O III] EW for galaxies around quasars with respect to the full sample. This aligns with recent results from J. B. Champagne et al. (2025) in another quasar field. As listed in Table 3, we measure very high overdensities for some quasars, while we can only report upper limits for other quasars, indicating significant scatter (see also F. Wang et al. 2023). For objects without companions within 1 cMpc, we list upper limits that would correspond to $N=2$ detected galaxies.

Combining these measurements with those presented in Section 4, we find correlations between the galaxy overdensity, broad Balmer line width, and BH mass, see Figure 14. As Balmer line width is used to derive BH mass, the two results are not independent of each other, but the relation appears slightly stronger when showing the directly observable quantity. We show the overdensity measured on 1 cMpc scales, but note that the trends are qualitatively similar on 2 cMpc scales. This correlation is in line with the result that more massive SMBHs reside in more massive galaxies (Figure 13), but it is also suggestive of a BH mass–halo mass relation, as more massive halos reside in larger overdensities.

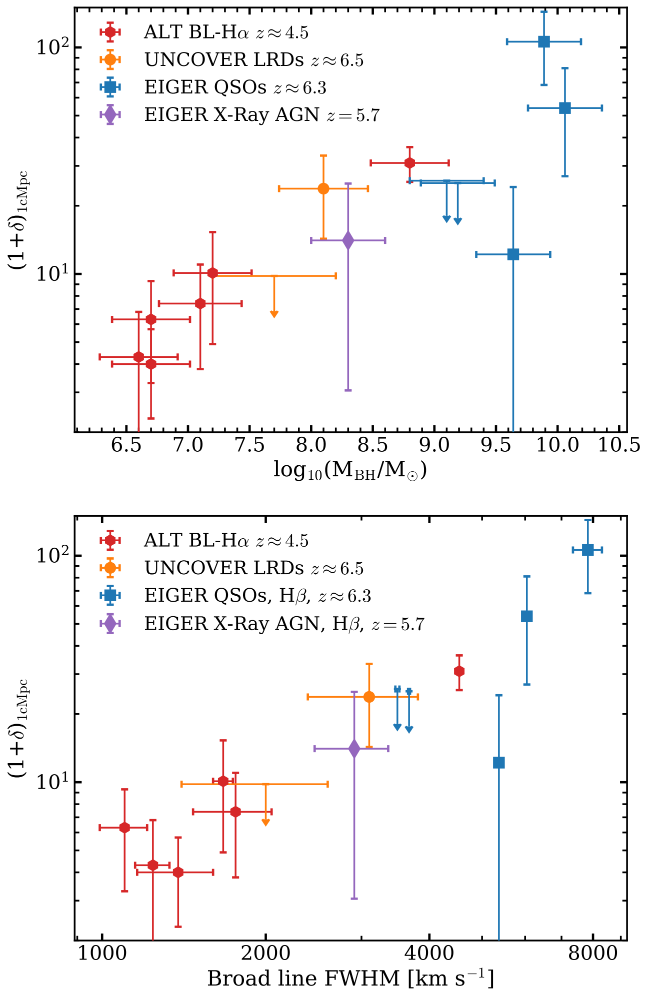

Figure 14. The relation between the overdensity (within 1 cMpc cylinders centered on the AGN) and BH mass (top) and broad Balmer line FWHM (bottom). Dark red hexagons show our results for the BL-Hα emitters at $z \approx 4.5$ from ALT, orange points are ALT overdensity measurements around NIRSpec-confirmed broad-line AGNs, blue squares show the results for the luminous quasars from the EIGER survey at $z \approx 6.3$, and the purple diamond is the overdensity around a UV-faint, X-ray-selected AGN at $z = 5.7$ covered by the EIGER survey.

Previous clustering measurements have yielded halo masses $\approx 2.5 \times 10^{12}\, M_\odot$ for the EIGER quasars (with BH mass $\sim 3 \times 10^9\, M_\odot$) using spectroscopic redshifts (A.-C. Eilers et al. 2024), while J. Arita et al. (2025) derived halo masses $\sim 6 \times 10^{11}\, M_\odot$ for broad-line-selected AGN (with BH mass $\sim 3 \times 10^7\, M_\odot$) using photometric redshifts. Assuming that our sample of BL-Hα emitters (with BH mass $\sim 6 \times 10^6\, M_\odot$) reside in typical dark matter halos given their stellar mass, their halo masses would be $\approx 5 \times 10^{10}\, M_\odot$ (e.g., P. Behroozi et al. 2019; M. Shuntov et al. 2022), but we caution that more detailed studies are required. Quantitatively establishing the shape of the BH mass–halo mass relation at redshift $z \sim 5$ directly would provide new constraints on models of SMBH formation and growth, and AGN feedback (e.g., R. G. Bower et al. 2017; H. Li et al. 2024; P. Dayal et al. 2025).

Various complications are involved in accurately quantifying such a BH mass–halo mass relation. The scatter in overdensities among individual halos at a given halo mass is substantial (e.g., Figure 12 of A. Torralba-Torregrosa et al. 2024). This challenges accurate individual halo mass inferences. Further, the galaxy samples that are used for overdensity measurements have different sensitivity limits and are at different redshifts, which could mean that their bias with respect to the matter density field varies (e.g., N. Dalmasso et al. 2024), which impacts halo mass inferences (e.g., E. Pizzati et al. 2024). Further, we note that Y. Shen et al. (2007) find much larger bias and halo masses for quasars at $z \sim 3$–4 than for quasars at $z \sim 6$ (A.-C. Eilers et al. 2024). While this could suggest strong redshift evolution, we note that the $z \sim 3$–4 halo mass measurements are much higher than both the $z \sim 2.5$ and $z \sim 6$ measurements, which is challenging to reconcile (see S. Eftekharzadeh et al. 2015 for a detailed discussion). Therefore, a future robust clustering analysis to quantify a possible BH mass–halo mass relation at $z \approx 5$–6 requires larger statistical samples of AGNs with consistent redshifts and overdensity probes. X. Lin et al. (2025) recently reported no significant correlation between the BH mass or BL FWHM and overdensity on 15 cMpc scales spectroscopically measured around BL-Hα emitters. This could imply that the trend in Figure 14 mainly traces nonlinear effects such as accelerated structure formation in relatively early collapsing environments.

7. Implications

7.1. The AGN Nature of BL-Hα Emitters

Due to the unusual spectrum of BL-Hα emitters, and especially due to their X-ray faintness (e.g., H. B. Akins et al. 2024; M. Yue et al. 2024a), some studies have questioned their AGN nature. The most common key indicator of AGN emission is currently broad Balmer line emission (but see also I. Labbe et al. 2024 for the detection of strong Fe II lines that unambiguously prove AGN activity). Theoretically, it is possible that broad Balmer lines may not originate from a BL region around an AGN, but might rather be due to a high velocity dispersion of gas in compact massive galaxies with high stellar densities (e.g., J. F. W. Baggen et al. 2024). In this scenario, the typical dispersion of ≈ 600 km s^{-1} of our sample would imply a stellar+gas mass of $\approx 3 \times 10^{10}\, M_\odot$ assuming a size of 100 pc, following the same methodology as described by J. F. W. Baggen et al. (2024) based on P. G. van Dokkum et al. (2015). As shown in Section 4, such a mass for the typical BL-Hα emitters in our sample would be strongly at odds with the measured overdensities (which would need to be about three times higher), unless the gas fractions were extremely high. Therefore, their overdensities rather point toward an AGN explanation for the broad Balmer line emission in the *typical* BL-Hα emitter. Note, however, as discussed above in Section 6, that some BL-Hα emitters could still reside in massive galaxies, but more evolved stellar populations are not the only cause of their red appearance.

7.2. A Luminosity-dependent Diversity in AGN Hosts

The trends between stellar mass, BH mass, and overdensities shown in Figures 13 and 14 imply that more luminous BL-Hα emitters reside in more massive galaxies, such that their SED will differ from that of the typical BL-Hα emitter from our sample. Indeed, we notice that ALT-66543, the most luminous and massive object in the sample with a strong Balmer break, has the reddest UV slope of $\beta = -0.7$, while the UV slopes of the others are much bluer, $\beta \approx -2$, implying an older or more obscured host galaxy and/or a stronger AGN contribution to the UV. UV-luminous quasars at

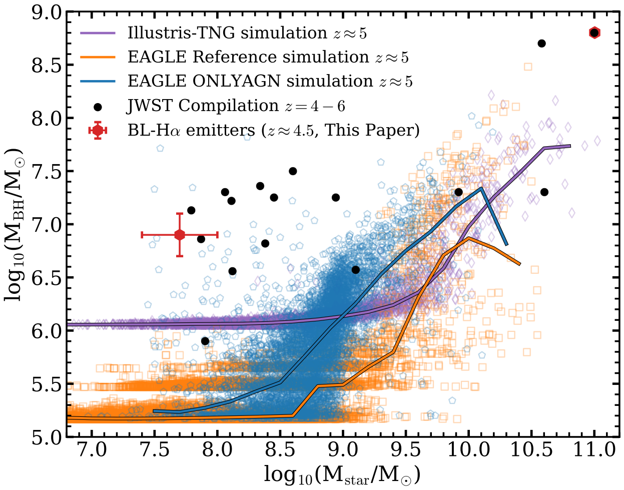

Figure 15. The relation between the stellar mass and supermassive black hole mass at $z \approx 5$, comparing measurements at $z \approx 5$ (dark red and black points from data as in Figure 13) with the 100 cMpc box EAGLE (R. A. Crain et al. 2015; J. Schaye et al. 2015) and Illustris-TNG (R. Weinberger et al. 2017; A. Pillepich et al. 2018) hydrodynamical simulations (orange and purple, respectively). Blue shows an EAGLE model without stellar feedback (ONLYAGN; with a 50 cMpc box size). Data points show individual galaxies. Solid lines show the running median. The seed SMBH masses are $\approx 10^5\,M_\odot$ and $\approx 10^6\,M_\odot$ in EAGLE and Illustris-TNG, respectively.

$z \approx 6$ with similar BH masses to ALT-66543 have also recently been shown to display Balmer breaks suggestive of older and massive galaxy populations (M. Onoue et al. 2024). However, if Balmer breaks may also arise from the AGN phenomena themselves (A. de Graaff et al. 2025b; K. Inayoshi & R. Maiolino 2025; X. Ji et al. 2025; R. P. Naidu et al. 2025), the relative stellar and AGN contributions may be challenging to disentangle. A natural consequence of such a luminosity-dependent diversity in AGN host galaxies is that different surveys may arrive at seemingly discrepant conclusions on the nature of BL-Hα emitters depending on their sensitivity and volumes covered. For example, BL-Hα emitters identified in deeper spectroscopic surveys will more likely reside in relatively low-mass galaxies, with blue UV slopes and without clear overdensities. Rarer and more luminous BL-Hα emitters, on the other hand, are more likely to reside in more massive galaxies with redder colors (e.g., B. Wang et al. 2024), larger overdensities, stronger Balmer breaks, and, possibly, a higher AGN contribution to the rest-frame UV emission.

7.3. Hydrodynamical Simulations Need to Grow SMBHs in Lower-mass Galaxies

State-of-the-art cosmological models of galaxy formation virtually all invoke the presence of AGN feedback associated with the growth of SMBHs to simulate realistic populations of galaxies (e.g., R. S. Somerville et al. 2008; R. A. Crain et al. 2015; R. Weinberger et al. 2017; R. Davé et al. 2019). These simulations are mostly tuned to reproduce properties of galaxy and cluster populations in the low-redshift Universe. However, the majority of SMBH seeding and growth occurs at high redshift, because models typically seed in relatively low-mass halos (e.g., Y. Rosas-Guevara et al. 2016) and massive galaxies form rapidly. In Figure 15, we show how the measured SMBH to stellar mass relation of the observed galaxies at $z \approx 5$ compares to the EAGLE (R. A. Crain et al. 2015; J. Schaye et al. 2015) and Illustris-TNG (R. Weinberger et al. 2017; A. Pillepich et al. 2018) hydrodynamical simulations.[23] We highlight that the stellar masses of AGNs with SMBHs with mass $\sim 10^7\,M_\odot$ are a factor 30–100 lower than the typical stellar masses that host such SMBHs in the Illustris-TNG and EAGLE Reference simulations (which are $\sim 5 \times 10^9\,M_\odot$, see the solid lines in Figure 15). In both simulations virtually all SMBHs in galaxies with masses $\approx 10^8\,M_\odot$ are still at the seed mass from the simulation, meaning that the simulations have not yet enabled their growth.

What would be needed to reconcile these differences? A key concern is the validity of the calibrations used to derive SMBH mass from broad Hα line width and luminosity. Given the X-ray faintness of JWST's broad Hα line emitters, it has been argued that they are experiencing super-Eddington accretion (e.g., E. Lambrides et al. 2024; F. Pacucci & R. Narayan 2024). Super-Eddington accretion is likely linked to a low AGN duty cycle due to the short duration of such inefficient bursts of SMBH growth. As discussed by E. Pizzati et al. (2025), the observed number densities of broad Hα line emitters at $z \sim 5$ can only be reconciled with a low ($\sim$1%) duty cycle if their halo masses are as low as $\sim 10^{11}\,M_\odot$. The number density of broad-line Hα emitters with implied BH masses $\sim 6 \times 10^6\,M_\odot$ (similar to our sources) is $\approx 2 \times 10^{-4}$ cMpc^{-3} (A. J. Taylor et al. 2025), while the galaxy stellar mass function yields number densities $\approx 2 \times 10^{-2}$ cMpc^{-3} for galaxies with stellar masses $\approx 5 \times 10^7\,M_\odot$ at these redshifts (e.g., C. C. Lovell et al. 2021; A. Weibel et al. 2024). This implies a duty cycle of 0.5%–1%. Therefore, the megaparsec-scale overdensities of the BL-Hα emitters are in agreement with this scenario where short bursts of super-Eddington accretion characterize the first stages of SMBH growth in low-mass halos. In the case of super-Eddington accretion, the standard single-epoch virial scaling relations used to infer SMBH masses might not be applicable, for example due to changes in the sizes of BL regions (A. Lupi et al. 2024). Although corrections for such effects are highly uncertain, they could imply SMBH masses an order of magnitude lower. Recently, V. Rusakov et al. (2025) and R. P. Naidu et al. (2025) proposed that radiative effects in dense gas around the AGNs (such as Thomson or resonant scattering) could broaden Balmer lines. Without accounting for such broadening, this would lead to overestimates of virial SMBH mass by up to 2 dex. However, the extent to which these effects are at play is under debate (I. Juodžbalis et al. 2025). Further, if line widths are primarily driven by radiative transfer effects, their correlation with overdensity (Figure 14) would be rather puzzling.

Given the large corrections of BH masses that would be required to reconcile the results shown in Figure 15, it is also justified to discuss possible changes in the models. R. A. Crain et al. (2015) and R. G. Bower et al. (2017) have shown how various model variations (in particular the seed mass, the feedback associated with star formation, and the parameters controlling the SMBH accretion rate) impact the BH to stellar mass relation in the EAGLE simulation. While they find that changes in the seed mass have a negligible impact, the strength of the stellar feedback controls the lowest mass at which SMBHs start their rapid growth (R. G. Bower et al. 2017; S. McAlpine et al. 2018; M. Trebitsch et al. 2018; H. Li et al. 2024). Additionally, allowing for super-Eddington accretion in simulations—not varied in EAGLE—likely leads to stronger BH growth than stellar mass growth (R. Schneider et al. 2023;

---

[23] See M. Habouzit et al. (2022) and M. Habouzit (2025) for a detailed comparison of EAGLE, Illustris-TNG and other cosmological simulations in the context of high-redshift SMBHs.

Y. Shi et al. 2023; J. S. Bennett et al. 2024; A. Trinca et al. 2024; S. Dattathri et al. 2025; F. Huško et al. 2025). This highlights the paradoxical twist that super-Eddington accretion could be a solution to create more massive SMBHs in simulations, yet its effect on the observed radiation could be to lower observationally inferred SMBH masses. Focusing on EAGLE, R. G. Bower et al. (2017) showed that rapid growth of SMBHs occurs as soon as they are seeded in the absence of stellar feedback. As we show in Figure 15, this ONLYAGN model without stellar feedback indeed leads to more efficient SMBH growth than stellar assembly, generally shifting the median BH–stellar mass relation to about 0.5 dex lower stellar masses. The variation in the ONLYAGN model produces a nonnegligible number of low-mass galaxies with BH to stellar mass ratios comparable to the observations, which indeed likely probe such a biased sample (J. Li et al. 2025). Therefore, a negligible efficiency of stellar feedback (at high redshift) would enable the formation of low-mass galaxies that host SMBHs with about 10% of their stellar mass, although such a model does not reproduce realistic galaxies at low redshift.

Finally, we remark that scenarios for feedback-free star formation in the early Universe have recently been explored in the context of the high abundance of UV-luminous galaxies at $z > 10$ (M. Castellano et al. 2022; R. P. Naidu et al. 2022; S. Carniani et al. 2024; C. M. Casey et al. 2024; Y. Harikane et al. 2025). As discussed by, e.g., A. Dekel et al. (2023), L. Mayer et al. (2025), and A. Renzini (2025), the high gas densities and low metallicities of halos in the early Universe could lead to a significantly higher star formation efficiency due to the decreased impact of feedback, and simultaneously promote the formation of intermediate-mass black holes and their efficient mergers into SMBHs (e.g., A. Dekel et al. 2025; L. Mayer et al. 2025). Thus, exploring such models in the context of a cosmological simulation that also reproduces galaxies at later times is highly warranted.

8. Summary

The population of faint AGNs at high redshift discovered in JWST data primarily through broad Hα line emission (a subset of this population presenting red colors and compact shapes has colloquially become known as the “Little Red Dots”) promises to unveil new insights into the formation and growth of SMBHs. A key measurement that is required to place these AGNs in context is their host stellar mass. Directly measuring stellar masses through fitting their SED is challenged because the AGN SEDs are complex and uncertain, and their contribution to the continuum is difficult to disentangle from stellar emission. Here, we perform an independent and empirical approach to infer the typical stellar mass of galaxies hosting broad Hα lines (BL-Hα emitters) at $z \approx 4$–5, based on comparing their megaparsec-scale environments to the environments around star-forming galaxies. We also explore correlations between BH mass, line width, and their large-scale environments. We primarily use BL-Hα emitters and galaxies identified using sensitive JWST/NIRCam grism data from the ALT survey behind the A2744 lensing cluster (R. P. Naidu et al. 2024), which benefits from a high spectroscopic completeness down to galaxy masses $\approx 10^7\,M_\odot$, accurate redshifts, and excellent imaging data to inform SED fits of the star-forming galaxies. Our main results are:

1. We identify a sample of six broad Hα line emitters at $z \approx 4$–5 with FWHM $> 1000\,\mathrm{km\,s^{-1}}$ and a luminosity $L_{\rm bol} > 10^{44.1}\,\mathrm{erg\,s^{-1}}$. Three of these were already confirmed as broad-line emitters from NIRSpec spectroscopy (J. E. Greene et al. 2024), including the exceptional ALT-66543, which is the most luminous Little Red Dot known (I. Labbe et al. 2024). The BL-Hα emitters have SMBHs with masses $10^{6.6-8.8}\,M_\odot$, typically $M_{\rm BH} = 10^{6.9}\,M_\odot$, and overlap in parameter space with typical JWST-identified AGNs. (Section 3.1, Figures 1 and 2, Table 1)
2. The ALT data show a large range in galaxy densities over the full ≈ 30 arcmin^2 field. BL-Hα emitters trace moderate galaxy overdensities and avoid the lowest-density regimes, but they avoid the most prominent overdensity. On 1 cMpc scales, the overdensities around the BL-Hα emitters are in the range $(1+\delta)_{1\,\rm cMpc} = 4$–30, typically $(1+\delta)_{1\,\rm cMpc} \approx 6$, excluding the exceptional ALT-66543. (Section 4, Figure 7, Table 1)
3. In the reference sample, we demonstrate that more massive galaxies are surrounded by more galaxies on 3–300 pkpc scales along the plane of the sky (and likely beyond). Within cylinders of $\Delta z/(1+z) = 0.005$ ($1500\,\mathrm{km\,s^{-1}}$), we find that the overdensity increases from $(1+\delta)_{1\,\rm cMpc} \approx 4$ for galaxies with stellar masses of $2 \times 10^7\,M_\odot$ to $(1+\delta)_{1\,\rm cMpc} \approx 10$ (13) at a mass of $\approx 10^{9(10)}\,M_\odot$. (Section 4, Figures 8, 10, and 12; Table 2)
4. We detect a clear and flat excess number of galaxy pairs below separations of ≈ 50 pkpc, which is due to satellites that cluster strongly within the typical virial radius of our galaxy sample. Based on a data-driven definition, we identify galaxies that are satellites to more massive galaxies and find satellite fractions of $\approx 30\%$ (15%) at $M_{\rm star} \approx 10^{8(9)}\,M_\odot$, and virtually zero above that. (Section 4.4, Figure 9)
5. Our estimates of the *relative* overdensity around galaxies of varying stellar mass are robust to our choice of Hα as a tracer. We demonstrate this by comparing Hα EW distributions around BL-Hα emitters and the reference sample galaxies, finding no difference on 1 cMpc scales (however, the AGNs show some signs of increased Hα EW at smaller $\lesssim 0.3$ cMpc scales). The Hα EW distributions also show that the most massive galaxies are surrounded by galaxies with lower Hα EWs and stronger Balmer breaks suggestive of accelerated evolution, possibly depressing their overdensity estimates. (Section 4.5, Figure 11)
6. We use the correlation between overdensity and stellar mass to infer that the typical BL-Hα emitter in our sample has a stellar mass of $10^{7.7\pm0.3}\,M_\odot$, ~ 1.5 dex lower than the median stellar mass inferred from galaxy-only SED fits. Taking the BH mass estimates based on single-epoch virial calibrations at face value, this implies a BH to stellar mass ratio as high as 12.5%, in line with earlier measurements, and in line with a slight 0.2 dex increase in the normalization of the local BH to stellar mass relation given our luminosity-limited selection effects. Interestingly, this stellar mass is similar to the mass one would infer from the UV luminosity for a typical mass-to-light ratio in the reference sample, but is lower by an order of magnitude in the rest-frame optical, indicating a significant AGN contribution to the rest-optical SED. (Section 5, Figure 13)
7. By extending our overdensity measurements to other samples of AGNs at $z \approx 6$ (from the EIGER and ALT surveys), we find an indication of a correlation between

the overdensity and BH mass, suggestive of a BH to halo mass relation. However, larger statistics of sensitive overdensity measurements are required to quantify this relation with uniform tracers. (Section 6, Figure 14, Table 3)

The main implications of our results are:

1. As the typical BL-Hα emitter in our sample resides in a moderate overdensity that is smaller than typical overdensities for galaxies with masses $\sim 10^{10}\,M_\odot$, our results disfavor alternative explanations of broad Hα lines that arise purely due to virial broadening of kinematics in very high stellar densities, at least for this study's sample that covers the lower-luminosity half of the literature samples. (Section 7.1, Figure 2)
2. The indicative correlation between BH mass and galaxy overdensity implies that we can expect a luminosity-dependent diversity among AGN hosts, with more massive and older host galaxies in more luminous quasars with heavier SMBHs. Statistical analyses of BL-Hα emitters, such as average clustering measurements, host galaxy mass or the shape of their SED, could thus be sensitive to the parameter space that AGNs occupy, which typically depends on survey characteristics. (Section 7.2)
3. Although current samples of BL-Hα emitters probe only a luminosity-limited subset of the SMBH population, the presence of AGNs in galaxies with stellar mass as low as $\approx 5 \times 10^7\,M_\odot$ and the high accompanying BH to stellar mass ratios are not seen in hydrodynamical models of galaxy formation. From the observational side, this could imply the BH masses are significantly overestimated, possibly due to short-lived super-Eddington accretion events, which would be in line with their low duty cycle and low masses. From the modeling side, the mechanisms controlling SMBH growth, such as the strength of stellar feedback, the maximum accretion rate or the seeding, may need to be revised, especially at early times. Interestingly, this highlights a possible common explanation for the presence of overly massive black holes in low-mass, high-redshift galaxies, and the high abundance of UV-luminous galaxies beyond $z > 10$. (Section 7.3, Figure 15)

Acknowledgments

We thank the referee for their constructive comments that helped to improve the paper. We thank Junyao Li for sharing model output shown in Figure 13, Rob Crain for sharing results from the ONLYAGN EAGLE model shown in Figure 15, and Adi Zitrin for comments. This work is based on observations made with the NASA/ESA/CSA James Webb Space Telescope. The data were obtained from the Mikulski Archive for Space Telescopes at the Space Telescope Science Institute, which is operated by the Association of Universities for Research in Astronomy, Inc., under NASA contract NAS 5-03127 for JWST. These observations are associated with programs # 3516. Funded by the European Union (ERC, AGENTS, 101076224). Views and opinions expressed are however those of the author(s) only and do not necessarily reflect those of the European Union or the European Research Council. Neither the European Union nor the granting authority can be held responsible for them. We acknowledge funding from JWST program GO-3516. Support for this work was provided by NASA through the NASA Hubble Fellowship grant HST-HF2-51515.001-A awarded by the Space Telescope Science Institute, which is operated by the Association of Universities for Research in Astronomy, Incorporated, under NASA contract NAS 5-26555. A.A. acknowledges support by the Swedish research council Vetenskapsrådet (2021-05559).

Facility: JWST.

Software: `Python`, `matplotlib` (J. D. Hunter 2007), `numpy` (C. R. Harris et al. 2020), `scipy` (P. Virtanen et al. 2020), `Astropy` (Astropy Collaboration et al. 2013, 2018).

Appendix A
Overdensities around All ALT BL-Hα Emitters

Figures 16 and 17 show the large-scale overdensities around the BL-Hα emitters that were not shown in the main text (Figure 7).

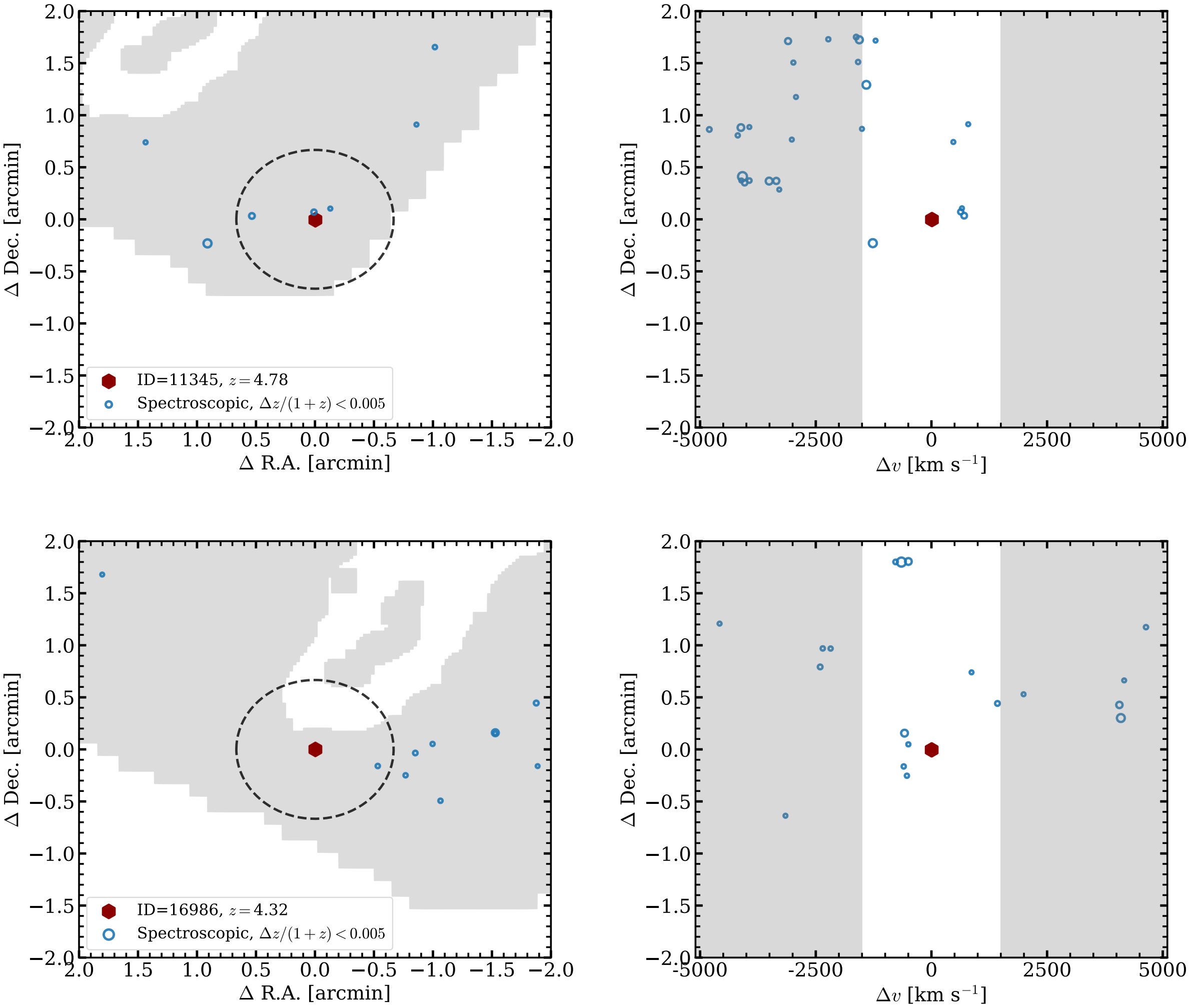

Figure 16. The environments of broad-line Hα emitters (as Figure 7).

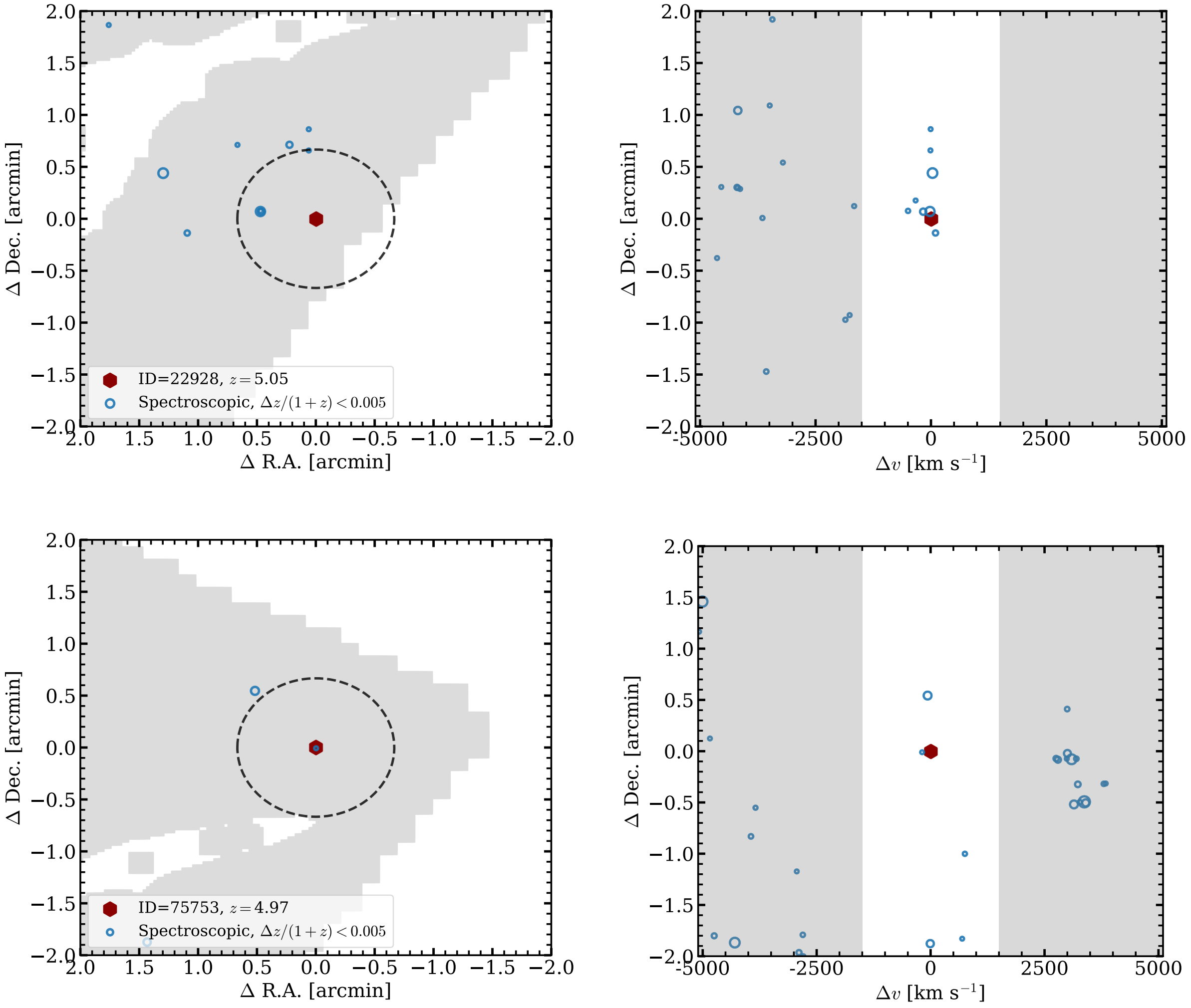

Figure 17. The environments of broad-line Hα emitters (as Figure 7).

Appendix B
Hα Profiles and SEDs of Suspected Broad-line Emitters

In Figures 18 and 19, we show the Hα spectra and the SEDs of ALT-ID 16772 (R.A., decl. = 3.57599, −30.41903, $z = 3.832$), 34016 (R.A., decl. = 3.604805, −30.369871, $z = 4.702$), and 62404 (R.A., decl. = 3.54772, −30.3337, $z = 4.867$), which we flagged as suspected/possible BLs in Figure 5, but for which the addition of a broad component does not significantly improve the fit (BIC improved by less than ΔBIC = 10; Table 4). ALT-16772, 34016, and 62404 are very faint galaxies with $M_{\rm UV} \approx -16$ to -17 with a compact appearance and a typical UV-blue, optical-red SED. They are particularly red given their faint continuum magnitude. Our sensitivity to broad Hα emission (BL flux of $\approx 10^{-18}$ erg s^{-1} cm^{-2} at $S/N \approx 5$) is probably preventing the significant detection of a broad component. These galaxies are in small overdensities, somewhat lower than the typical BL-Hα emitters in the sample.

In Figure 20, we focus specifically on ALT-62975 (R.A., decl. = 3.56574, −30.33597, $z = 3.98$), which was also flagged as a possible BL-Hα emitter in the main text. The main reason why broad Hα emission is suspected is the atypical line profile shown in the left panel of Figure 20. This profile could be ascribed to a strong absorber on top of a broad Hα profile, similar to some extreme BL-Hα emitters identified in NIRCam grism data (J. Matthee et al. 2024) and NIRSpec data (e.g., I. Juodžbalis et al. 2024a; F. D'Eugenio et al. 2025). However, such a fit would have worse χ^2 and BIC ($\chi^2 = 2.50$, BIC = 141) than fits with a single or a two-component Gaussian emission model. Instead, we find that the Hα profile of ALT-62975 is best characterized by very strong [N II] emission ([N II]/Hα = 0.95 ± 0.10), with only a very small improvement in fitting statistics when adding a broad component (see Table 4).

ALT-62975 is among the most luminous systems in the ALT catalog at z = 4–5, has very red colors, and its SED suggests that it is a very massive galaxy with a stellar mass $4 \times 10^{10}\,M_\odot$. While the galaxy appears compact, it is slightly extended in the rest-frame optical, suggesting that a significant fraction of the rest-frame optical light is stellar. This suggests that the [N II] + Hα emission traces gas that is shock-ionized (possibly by AGN activity), similar to that observed in various other massive evolved galaxies at $z \gtrsim 4$ (e.g., A. de Graaff et al. 2025c). The galaxy resides in a large overdensity, providing further evidence that stellar light is the dominant contribution to the SED.

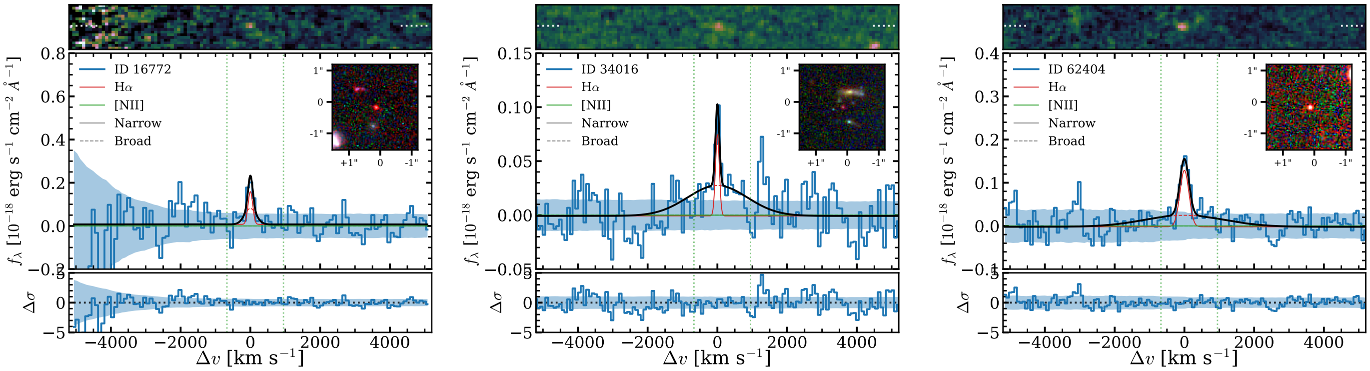

Figure 18. The Hα profiles of the three suspected broad-line emitters (as Figure 1). Top panels show the 2D continuum-subtracted grism spectra. The middle panels show the optimally extracted 1D spectra. Blue lines show the data, where shaded regions show the errors. The black line shows the combined fit that is composed of a narrow Hα line and a broad one and narrow [N II]. The red dashed and solid components show the broad and narrow Hα components and green shows the best-fit [N II] line, whose wavelength we highlight with dotted green lines. Bottom panels show the residuals of the spectral fit. Inset panels show pseudo-RGB images constructed from NIRCam F115W/F200W/F356W images, highlighting the point-source morphology of the objects.

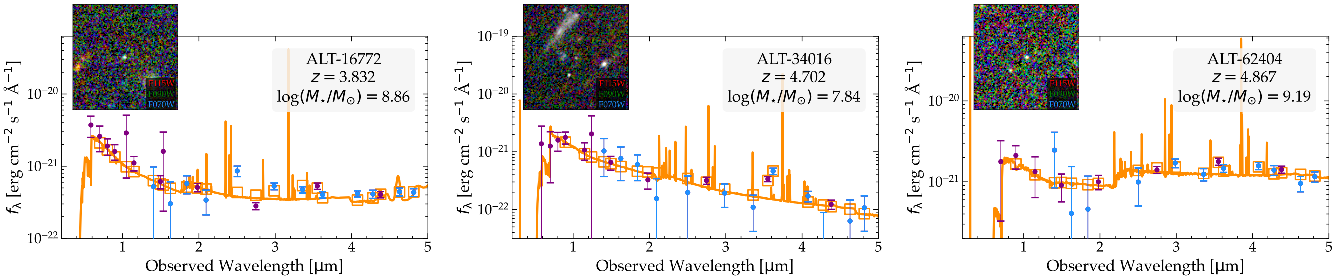

Figure 19. SED fits of the three suspected BL-Hα emitters (as Figure 3). Orange curves and shaded regions show the best-fit SEDs *assuming pure stellar and nebular emission* and their uncertainties that ignore an AGN contribution. Purple data points are measurements in broadband filters, while blue data points are medium-band filters. Inset stamps are false-color RGB images of 2.″4 × 2.″4 based on the F070W, F090W, and F115W NIRCam imaging data.

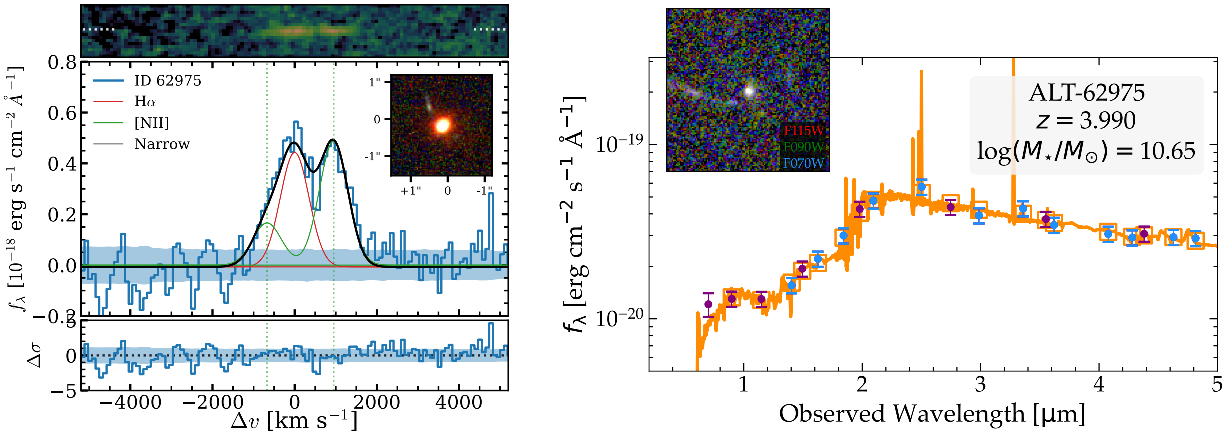

Figure 20. Left: the best-fit Hα + [N II] fit for ALT-62975 (as Figure 18, where the inset panel is rotated by the position angle of the grism observations). Unlike other BL-Hα emitters, this profile is best fitted as an object with a high [N II]/Hα ratio indicative of shock ionization. Right: the SED fit of ALT-62975, as Figure 19, which shows that the SED is well described by a massive evolved galaxy (here, the inset panel highlights the rest-UV morphology in NE orientation).

Table 4
Hα Line Profile Fitting Statistics

ALT-ID	$\chi^2_{\rm single}$	$\chi^2_{\rm two}$	BIC$_{\rm single}$	BIC$_{\rm broad}$	S/N Hα$_{\rm broad}$
Confirmed BL-Hα					
11345	2.05	1.53	126.2	89.7	8.9
16986	4.30	1.90	212.1	112.4	24.2
22928	2.91	2.48	181.5	162.2	8.7
66543[a]	67.6	22.4	643.0	485.5	139.2
69688	16.84	4.11	382.5	208.5	43.2
75753	4.03	2.17	225.3	141.3	17.7
Suspected BL-Hα					
16772	1.77	1.71	91.8	91.7	1.7
34016	3.29	3.10	189.1	185.3	3.2
62404	1.32	1.25	65.5	62.0	2.1
62975	1.61	1.60	86.1	85.5	2.3

Note. Reduced χ^2 and BIC values are shown for the best fits of the Hα + [N II] models with a single or two-component Gaussian model, and the S/N of the broad Hα flux in the two-component model.

[a] The Hα profile of ALT-66543 is best described with a more complicated model that includes absorption and a Lorentzian broad wing, as explained by I. Labbe et al. (2024).

ORCID iDs

Jorryt Matthee https://orcid.org/0000-0003-2871-127X
Rohan P. Naidu https://orcid.org/0000-0003-3997-5705
Gauri Kotiwale https://orcid.org/0009-0007-1062-0253
Lukas J. Furtak https://orcid.org/0000-0001-6278-032X
Ivan Kramarenko https://orcid.org/0000-0001-5346-6048
Ruari Mackenzie https://orcid.org/0000-0003-0417-385X
Jenny Greene https://orcid.org/0000-0002-5612-3427
Angela Adamo https://orcid.org/0000-0002-8192-8091
Rychard J. Bouwens https://orcid.org/0000-0002-4989-2471
Claudia Di Cesare https://orcid.org/0000-0003-1408-7373
Anna-Christina Eilers https://orcid.org/0000-0003-2895-6218
Anna de Graaff https://orcid.org/0000-0002-2380-9801
Kasper E. Heintz https://orcid.org/0000-0002-9389-7413
Daichi Kashino https://orcid.org/0000-0001-9044-1747
Michael V. Maseda https://orcid.org/0000-0003-0695-4414
Sandro Tacchella https://orcid.org/0000-0002-8224-4505
Alberto Torralba https://orcid.org/0000-0001-5586-6950

References

Adamo, A., Atek, H., Bagley, M. B., et al. 2024, arXiv:2405.21054
Akins, H. B., Casey, C. M., Berg, D. A., et al. 2025, ApJL, 980, L29
Akins, H. B., Casey, C. M., Lambrides, E., et al. 2024, arXiv:2406.10341
Ananna, T. T., Bogdán, Á., Kovács, O. E., Natarajan, P., & Hickox, R. C. 2024, ApJL, 969, L18
Arita, J., Kashikawa, N., Onoue, M., et al. 2025, MNRAS, 536, 3677
Astropy Collaboration, Price-Whelan, A. M., Sipőcz, B. M., et al. 2018, AJ, 156, 123
Astropy Collaboration, Robitaille, T. P., Tollerud, E. J., et al. 2013, A&A, 558, A33
Baggen, J. F. W., van Dokkum, P., Brammer, G., et al. 2024, ApJL, 977, L13
Behroozi, P., Wechsler, R. H., Hearin, A. P., & Conroy, C. 2019, MNRAS, 488, 3143
Bennett, J. S., Sijacki, D., Costa, T., Laporte, N., & Witten, C. 2024, MNRAS, 527, 1033
Bezanson, R., Labbe, I., Whitaker, K. E., et al. 2024, ApJ, 974, 92
Blumenthal, G. R., Faber, S. M., Primack, J. R., & Rees, M. J. 1984, Natur, 311, 517
Bordoloi, R., Simcoe, R. A., Matthee, J., et al. 2024, ApJ, 963, 28
Bower, R. G., Schaye, J., Frenk, C. S., et al. 2017, MNRAS, 465, 32
Brooks, M., Simons, R. C., Trump, J. R., et al. 2025, ApJ, 986, 177
Carnall, A. C., McLure, R. J., Dunlop, J. S., et al. 2023, Natur, 619, 716
Carniani, S., Hainline, K., D'Eugenio, F., et al. 2024, Natur, 633, 318
Casey, C. M., Akins, H. B., Shuntov, M., et al. 2024, ApJ, 965, 98
Castellano, M., Fontana, A., Treu, T., et al. 2022, ApJL, 938, L15
Champagne, J. B., Wang, F., Yang, J., et al. 2025, ApJ, 981, 114
Chen, C.-H., Ho, L. C., Li, R., & Zhuang, M. Y. 2025, ApJ, 983, 60
Covelo-Paz, A., Giovinazzo, E., Oesch, P. A., et al. 2025, A&A, 694, 178
Crain, R. A., Schaye, J., Bower, R. G., et al. 2015, MNRAS, 450, 1937
Dalmasso, N., Leethochawalit, N., Trenti, M., & Boyett, K. 2024, MNRAS, 533, 2391
Dattathri, S., Natarajan, P., Porras-Valverde, A. J., et al. 2025, ApJ, 984, 122
Davé, R., Anglés-Alcázar, D., Narayanan, D., et al. 2019, MNRAS, 486, 2827
Dayal, P., Volonteri, M., Greene, J. E., et al. 2025, A&A, 697, A211
de Graaff, A., Brammer, G., Weibel, A., et al. 2025a, A&A, 697, A189
de Graaff, A., Rix, H.-W., Naidu, R. P., et al. 2025b, arXiv:2503.16600
de Graaff, A., Setton, D. J., Brammer, G., et al. 2025c, NatAs, 9, 280
Dekel, A., Sarkar, K. C., Birnboim, Y., Mandelker, N., & Li, Z. 2023, MNRAS, 523, 3201
Dekel, A., Stone, N. C., Chowdhury, D. D., et al. 2025, A&A, 695, A97
D'Eugenio, F., Maiolino, R., Perna, M., et al. 2025, arXiv:2503.11752
D'Eugenio, F., Pérez-González, P. G., Maiolino, R., et al. 2024, NatAs, 8, 1443
Diemer, B. 2018, ApJS, 239, 35
Ding, X., Onoue, M., Silverman, J. D., et al. 2023, Natur, 621, 51
Eftekharzadeh, S., Myers, A. D., White, M., et al. 2015, MNRAS, 453, 2779
Eilers, A.-C., Mackenzie, R., Pizzati, E., et al. 2024, ApJ, 974, 275
Eilers, A.-C., Simcoe, R. A., Yue, M., et al. 2023, ApJ, 950, 68
Fan, X., Bañados, E., & Simcoe, R. A. 2023, ARA&A, 61, 373
Fujimoto, S., Brammer, G. B., Watson, D., et al. 2022, Natur, 604, 261
Furtak, L. J., Labbé, I., Zitrin, A., et al. 2024, Natur, 628, 57
Furtak, L. J., Zitrin, A., Weaver, J. R., et al. 2023, MNRAS, 523, 4568
Goulding, A. D., Greene, J. E., Setton, D. J., et al. 2023, ApJL, 955, L24
Greene, J. E., & Ho, L. C. 2005, ApJ, 630, 122
Greene, J. E., Labbe, I., Goulding, A. D., et al. 2024, ApJ, 964, 39
Habouzit, M. 2025, MNRAS, 537, 2323
Habouzit, M., Onoue, M., Bañados, E., et al. 2022, MNRAS, 511, 3751
Haiman, Z. 2013, in The First Galaxies, ed. T. Wiklind, B. Mobasher, & V. Bromm (Berlin: Springer), 293
Hainline, K. N., Maiolino, R., Juodžbalis, I., et al. 2025, ApJ, 979, 138
Harikane, Y., Inoue, A. K., Ellis, R. S., et al. 2025, ApJ, 980, 138
Harikane, Y., Zhang, Y., Nakajima, K., et al. 2023, ApJ, 959, 39
Harris, C. R., Millman, K. J., van der Walt, S. J., et al. 2020, Natur, 585, 357
Helton, J. M., Sun, F., Woodrum, C., et al. 2024, ApJ, 962, 124
Herard-Demanche, T., Bouwens, R. J., Oesch, P. A., et al. 2025, MNRAS, 537, 788
Herrero Alonso, Y., Miyaji, T., Wisotzki, L., et al. 2023, A&A, 671, A5
Hunter, J. D. 2007, CSE, 9, 90
Huško, F., Lacey, C. G., Roper, W. J., et al. 2025, MNRAS, 537, 2559
Inayoshi, K., & Maiolino, R. 2025, ApJL, 980, L27
Ji, X., Maiolino, R., Übler, H., et al. 2025, arXiv:2501.13082
Juodžbalis, I., Ji, X., Maiolino, R., et al. 2024a, MNRAS, 535, 853
Juodžbalis, I., Maiolino, R., Baker, W. M., et al. 2024b, Natur, 636, 594
Juodžbalis, I., Maiolino, R., Baker, W. M., et al. 2025, arXiv:2504.03551
Kashino, D., Lilly, S. J., Matthee, J., et al. 2023, ApJ, 950, 66
Kashino, D., Lilly, S. J., Matthee, J., et al. 2025, arXiv:2506.03121
Katz, H., Cameron, A. J., Saxena, A., et al. 2024, arXiv:2408.03189
Killi, M., Watson, D., Brammer, G., et al. 2024, A&A, 691, A52
Kocevski, D. D., Barro, G., McGrath, E. J., et al. 2023a, ApJL, 946, L14
Kocevski, D. D., Finkelstein, S. L., Barro, G., et al. 2025, ApJ, 986, 126
Kocevski, D. D., Onoue, M., Inayoshi, K., et al. 2023b, ApJL, 954, L4
Kokorev, V., Chisholm, J., Endsley, R., et al. 2024, ApJ, 975, 178
Kokorev, V., Fujimoto, S., Labbe, I., et al. 2023, ApJL, 957, L7
Labbé, I., van Dokkum, P., Nelson, E., et al. 2023, Natur, 616, 266
Labbe, I., Greene, J. E., Bezanson, R., et al. 2025, ApJ, 978, 92
Labbe, I., Greene, J. E., Matthee, J., et al. 2024, arXiv:2412.04557
Lambrides, E., Garofali, K., Larson, R., et al. 2024, arXiv:2409.13047
Larson, R. L., Finkelstein, S. L., Kocevski, D. D., et al. 2023, ApJL, 953, L29
Leung, G. C. K., Finkelstein, S. L., Pérez-González, P. G., et al. 2024, arXiv:2411.12005
Li, H., Chen, Y., Wang, H., & Mo, H. 2024, arXiv:2409.06208
Li, J., Silverman, J. D., Shen, Y., et al. 2025, ApJ, 981, 19
Lin, X., Fan, X., Sun, F., et al. 2025, arXiv:2505.02896
Lin, X., Wang, F., Fan, X., et al. 2024, ApJ, 974, 147
Lovell, C. C., Vijayan, A. P., Thomas, P. A., et al. 2021, MNRAS, 500, 2127
Lupi, A., Trinca, A., Volonteri, M., Dotti, M., & Mazzucchelli, C. 2024, A&A, 689, A128

Ma, Y., Greene, J. E., Setton, D. J., et al. 2025, ApJ, 981, 191
Mahabal, A., Stern, D., Bogosavljević, M., Djorgovski, S. G., & Thompson, D. 2005, ApJL, 634, L9
Maiolino, R., Risaliti, G., Signorini, M., et al. 2025, MNRAS, 538, 1921
Maiolino, R., Scholtz, J., Curtis-Lake, E., et al. 2024a, A&A, 691, A145
Maiolino, R., Scholtz, J., Witstok, J., et al. 2024b, Natur, 627, 59
Marshall, M. A., Yue, M., Eilers, A.-C., et al. 2024, arXiv:2410.11035
Matthee, J., Mackenzie, R., Simcoe, R. A., et al. 2023, ApJ, 950, 67
Matthee, J., Naidu, R. P., Brammer, G., et al. 2024, ApJ, 963, 129
Mayer, L., van Donkelaar, F., Messa, M., Capelo, P. R., & Adamo, A. 2025, ApJL, 981, L28
McAlpine, S., Bower, R. G., Rosario, D. J., et al. 2018, MNRAS, 481, 3118
McConachie, I., Wilson, G., Forrest, B., et al. 2025, ApJ, 978, 17
Morishita, T., Liu, Z., Stiavelli, M., et al. 2025, ApJ, 982, 153
Naidu, R., & Matthee, J. 2024, All the Little Things (ALT) Data Release 1, v1, Zenodo, doi:10.5281/zenodo.13871850
Naidu, R. P., Matthee, J., Katz, H., et al. 2025, arXiv:2503.16596
Naidu, R. P., Matthee, J., Kramarenko, I., et al. 2024, arXiv:2410.01874
Naidu, R. P., Oesch, P. A., van Dokkum, P., et al. 2022, ApJL, 940, L14
Napolitano, L., Castellano, M., Pentericci, L., et al. 2025, A&A, 693, A50
Natarajan, P., Pacucci, F., Ricarte, A., et al. 2024, ApJL, 960, L1
Oesch, P. A., Brammer, G., Naidu, R. P., et al. 2023, MNRAS, 525, 2864
Onoue, M., Ding, X., Silverman, J. D., et al. 2024, arXiv:2409.07113
Ortega-Martinez, S., Contreras, S., Angulo, R. E., & Chaves-Montero, J. 2025, A&A, 697, A226
Pacucci, F., & Narayan, R. 2024, ApJ, 976, 96
Pacucci, F., Nguyen, B., Carniani, S., Maiolino, R., & Fan, X. 2023, ApJL, 957, L3
Pérez-González, P. G., Barro, G., Rieke, G. H., et al. 2024, ApJ, 968, 4
Pillepich, A., Springel, V., Nelson, D., et al. 2018, MNRAS, 473, 4077
Pizzati, E., Hennawi, J. F., Schaye, J., et al. 2024, MNRAS, 534, 3155
Pizzati, E., Hennawi, J. F., Schaye, J., et al. 2025, MNRAS, 539, 2910
Planck Collaboration, Aghanim, N., Akrami, Y., et al. 2020, A&A, 641, A6
Price, S. H., Bezanson, R., Labbe, I., et al. 2025, ApJ, 982, 51
Reines, A. E., Greene, J. E., & Geha, M. 2013, ApJ, 775, 116
Reines, A. E., & Volonteri, M. 2015, ApJ, 813, 82
Renzini, A. 2025, MNRAS, 536, L8
Richards, G. T., Lacy, M., Storrie-Lombardi, L. J., et al. 2006, ApJS, 166, 470
Rosas-Guevara, Y., Bower, R. G., Schaye, J., et al. 2016, MNRAS, 462, 190
Rusakov, V., Watson, D., Nikopoulos, G. P., et al. 2025, arXiv:2503.16595
Schaye, J., Crain, R. A., Bower, R. G., et al. 2015, MNRAS, 446, 521
Schindler, J.-T., Hennawi, J. F., Davies, F. B., et al. 2024, arXiv:2411.11534
Schneider, R., Valiante, R., Trinca, A., et al. 2023, MNRAS, 526, 3250
Scholtz, J., Maiolino, R., D'Eugenio, F., et al. 2025, A&A, 697, A175
Setton, D. J., Greene, J. E., de Graaff, A., et al. 2024a, arXiv:2411.03424
Setton, D. J., Khullar, G., Miller, T. B., et al. 2024b, ApJ, 974, 145
Shen, Y., Strauss, M. A., Oguri, M., et al. 2007, AJ, 133, 2222
Shi, Y., Kremer, K., Grudić, M. Y., Gerling-Dunsmore, H. J., & Hopkins, P. F. 2023, MNRAS, 518, 3606
Shuntov, M., Ilbert, O., Toft, S., et al. 2025a, A&A, 695, A20
Shuntov, M., McCracken, H. J., Gavazzi, R., et al. 2022, A&A, 664, A61
Shuntov, M., Oesch, P. A., Toft, S., et al. 2025b, A&A, 699, A231
Somerville, R. S., Barden, M., Rix, H., et al. 2008, ApJ, 672, 776
Stepney, M., Banerji, M., Tang, S., et al. 2024, MNRAS, 533, 2948
Suess, K. A., Weaver, J. R., Price, S. H., et al. 2024, ApJ, 976, 101
Sun, F., Helton, J. M., Egami, E., et al. 2024, ApJ, 961, 69
Tanaka, T. S., Silverman, J. D., Shimasaku, K., et al. 2024, arXiv:2412.14246
Taylor, A. J., Finkelstein, S. L., Kocevski, D. D., et al. 2025, ApJ, 986, 165, arXiv:2409.06772
Torralba-Torregrosa, A., Matthee, J., Naidu, R. P., et al. 2024, A&A, 689, A44
Trebitsch, M., Volonteri, M., Dubois, Y., & Madau, P. 2018, MNRAS, 478, 5607
Treiber, H., Greene, J. E., Weaver, J. R., et al. 2025, ApJ, 984, 93
Trinca, A., Valiante, R., Schneider, R., et al. 2024, arXiv:2412.14248
van Dokkum, P. G., Nelson, E. J., Franx, M., et al. 2015, ApJ, 813, 23
Virtanen, P., Gommers, R., Oliphant, T. E., et al. 2020, NatMe, 17, 261
Volonteri, M., Trebitsch, M., Greene, J. E., et al. 2025, A&A, 695, A33
Wang, B., de Graaff, A., Davies, R. L., et al. 2025, ApJ, 984, 121
Wang, B., Leja, J., de Graaff, A., et al. 2024, ApJL, 969, L13
Wang, F., Yang, J., Hennawi, J. F., et al. 2023, ApJL, 951, L4
Weibel, A., de Graaff, A., Setton, D. J., et al. 2025, ApJ, 983, 11
Weibel, A., Oesch, P. A., Barrufet, L., et al. 2024, MNRAS, 533, 1808
Weinberger, R., Springel, V., Hernquist, L., et al. 2017, MNRAS, 465, 3291
Williams, C. C., Alberts, S., Ji, Z., et al. 2024, ApJ, 968, 34
Wu, X.-B., Wang, F., Fan, X., et al. 2015, Natur, 518, 512
Yue, M., Eilers, A.-C., Ananna, T. T., et al. 2024a, ApJL, 974, L26
Yue, M., Eilers, A.-C., Simcoe, R. A., et al. 2024b, ApJ, 966, 176
Zhang, H., Behroozi, P., Volonteri, M., et al. 2023, MNRAS, 523, L69